Tsunami generation by a rapid entrance of pyroclastic flow into the sea during the 1883 Krakatau eruption, Indonesia

Fukashi Maeno[1,2] and Fumihiko Imamura[3]

Received 21 January 2011; revised 14 June 2011; accepted 29 June 2011; published 23 September 2011.

[1] The 1883 eruption of Krakatau volcano in Indonesia was one of the most explosive volcanic events in history. It was a marine caldera-forming eruption that resulted in voluminous ignimbrite deposits and huge tsunamis. We have used numerical simulations to investigate three major mechanisms for tsunami generation: caldera collapse, phreatomagmatic explosion, and pyroclastic flow, and have constrained the source parameters. Computed tsunami characteristics for each hypothesis are compared with observations at locations along the coasts of the Sunda Strait, where tsunami data were obtained immediately after the eruption. For the pyroclastic flow hypothesis, two types of two-layer shallow water models, dense- and light-type models, were used under different initial conditions. Pyroclastic flows are erupted from a circular source following a sine function that assumes waning and waxing phases. Caldera collapse was performed using a simple piston-like plunger model, in which collapse duration was assumed to be up to 1 h. The phreatomagmatic explosion hypothesis was examined using simple empirical models for underwater explosions in shallow water, with explosion energy between 10^{16} and 10^{17} J. The results show that when a pyroclastic flow with a volume of >5 km^3 and an average discharge rate of the order of 10^7 m^3/s enters the sea, the computed tsunami heights are broadly consistent with historical records in coastal areas, including a tide gauge record at Batavia (now Jakarta). We conclude that a pyroclastic flow entering the sea is the most plausible mechanism of the 1883 Krakatau tsunami.

Citation: Maeno, F., and F. Imamura (2011), Tsunami generation by a rapid entrance of pyroclastic flow into the sea during the 1883 Krakatau eruption, Indonesia, *J. Geophys. Res.*, *116*, B09205, doi:10.1029/2011JB008253.

1. Introduction

[2] Large-scale volcanic events such as caldera-forming eruptions and volcanic landslides can cause serious natural hazards on the earth's surface. In the ocean, they have a great potential to create devastating tsunamis [e.g., *Latter*, 1981; *Beget*, 2000] that could extensively impact coastal societies and the natural environment. Some recent studies have attempted to characterize tsunamis triggered by such large-scale volcanic events and determine their source conditions [e.g., *Waythomas and Neal*, 1998; *Waythomas and Watts*, 2003; *Maeno et al.*, 2006; *Maeno and Imamura*, 2007]. However, quantitative constraints remain uncertain because of indirect observations, limited geological data, and difficulties in geophysical monitoring that aims to capture the details of such processes.

[3] The 1883 eruption of Krakatau in Indonesia is one of the most recent marine caldera-forming eruptions. The scale of the eruption was (Volcano Explosive Index) VEI 6, and it was accompanied by the production of a voluminous ignimbrite and huge tsunamis. The death toll, most of which occurred as a result of a tsunami during the climactic phase of the eruption, exceeded 36,000 [*Simkin and Fiske*, 1983]. The northern part of the old Rakata island disappeared and was replaced by a caldera that is about 270 m deep [*Sigurdsson et al.*, 1991]; an ignimbrite shallowed the bathymetry around Krakatau. The runup height of the tsunami is thought to have reached over 30 m as it broke along the coasts of the Sunda Strait [*Verbeek*, 1885; *Symons*, 1888; *Self and Rampino*, 1981]. Geological evidences of the tsunami have also been observed along some coastlines in neighboring islands [*Carey et al.*, 2001] and in marine sediments at Teluk Banten, Java [*van den Bergh et al.*, 2003].

[4] This eruption provides a good data set with which to investigate generation mechanisms of catastrophic volcanogenic tsunamis, as well as to determine source conditions for such events. This eruption significantly and devastatingly affected the development of coastal human activities and environments around Krakatau, and therefore many studies have been undertaken to examine this catastrophic tsunami event [e.g., *Self and Rampino*, 1981; *Yokoyama*, 1981, 1987; *Camus and Vincent*, 1983; *Francis*, 1985; *Sigurdsson et al.*, 1991; *Nomanbhoy and Satake*, 1995; *Carey et al.*, 2000; *De Lange et al.*, 2001]. However, speculation and controversy abound, particularly with respect to the generation mechanism of the tsunami for which the following three major hypotheses have been proposed: (1) caldera collapse,

[1]Department of Earth Sciences, University of Bristol, Bristol, UK.
[2]Earthquake Research Institute, University of Tokyo, Tokyo, Japan.
[3]Disaster Control Research Center, Graduate School of Engineering, Tohoku University, Sendai, Japan.

0148-0227/11/2011JB008253

(2) phreatomagmagtic explosion, and (3) pyroclastic flow entering the sea, as described below.

[5] 1. The caldera collapse hypothesis for a devastating tsunami assumes a sudden subsidence of an old volcanic edifice, associated with the evacuation of a large amount of magma [*Verbeek*, 1885; *Francis*, 1985; *Sigurdsson et al.*, 1991]. However, the computed waveform with a negative first arrival does not match the observed tsunami that had a positive first arrival, as recorded at a tide-gauge station at Batavia (now Jakarta) [*Nomanbhoy and Satake*, 1995]. Another study pointed out that if caldera collapse occurred very rapidly, with <10 s of free fall, then the first negative peak may be captured by a second positive peak due to the effect of the shallower bathymetry in the proximal area, resulting in the observed first positive peak arrival at Batavia [*Kawamata et al.*, 1993]. However, such rapid collapse is unlikely to have occurred, because the actual caldera collapse duration has been estimated to have been on the order of hours (e.g., the Pinatubo eruption [*Wolfe and Hoblitt*, 1996]) to days (e.g., the Bishop Tuff eruption [*Wilson and Hildreth*, 1997]). Numerical simulation of tsunamis during the 7.3 ka Kikai eruption, Japan, also demonstrated that the duration of caldera collapse could be on the order of hours [*Maeno et al.*, 2006; *Maeno and Imamura*, 2007]. The modeling similarly indicated that caldera collapse is unlikely to have produced the observed tsunamis.

[6] 2. The submarine phreatomagmatic explosion hypothesis was suggested by *Yokoyama* [1981, 1987] and *Nomanbhoy and Satake* [1995]. *Yokoyama* [1987] proposed that the tsunami was generated by a series of surge-producing explosions occurring over a 30-min period, which then coalesced to create an initial large wave. *Nomanbhoy and Satake* [1995] numerically simulated this hypothesis using a water surface elevation model. They assumed an initial upward displacement of ~10 km^3 of water formed by a huge explosion with water displaced upward over a period of 1 to 5 min as if it were pushed up by a piston. However, there is no detailed discussion to support this initial condition for a phreatomagmatic explosion, and they were not able to reproduce the observed tsunami using different initial conditions with longer explosion periods on the order of ten minutes. In general, the formation of a water dome or a water crater by an underwater explosion should occur very rapidly, particularly in cases occurring in a shallow sea with a high-energy explosion. In such a case, the explosion site would be almost completely evacuated within a few seconds [*Le Mehaute and Wang*, 1996]. Earlier assessments of the phreatomagmatic explosion hypothesis contradict the fundamental physics of such an explosion. Moreover, the mechanism proposed by *Yokoyama* [1981, 1987] does not account for required geological features. The submarine deposits in the vicinity of Krakatau were mainly composed of pumice and ash (>90% by volume), and there is little evidence of non-juvenile lithic fragments derived from old volcanic edifices, which should have been produced by such an explosive phreatomagmatic eruption [*Self and Rampino*, 1982; *Sigurdsson et al.*, 1991; *Mandeville et al.*, 1996; *Carey et al.*, 1996]. *Deplus et al.* [1995] also suggested that a depressed area on the seafloor of Krakatau shows a typical caldera produced by a sudden collapse of volcanic edifices, rather than an explosion crater.

[7] 3. The pyroclastic flow hypothesis suggests that a large discharge of a pyroclastic material into sea at the Krakatau volcano could trigger the generation of tsunamis [*Latter*, 1981; *Self and Rampino*, 1981; *Carey et al.*, 1996, 2000; *De Lange et al.*, 2001]. However, the details of interactions between a pyroclastic flow and seawater have not been investigated before, although pyroclastic flows entering water have been theoretically and experimentally studied recently [*McLeod et al.*, 1999; *Monaghan et al.*, 1999; *Legros and Druitt*, 2000; *Freundt*, 2003; *Watts and Waythomas*, 2003; *Dufek et al.*, 2007]. *Nomanbhoy and Satake* [1995] used the initial condition of a simple linear decrease in bathymetry due to an emplacement of a pyroclastic flow, but it is not based on the physics of flow-water interaction. According to eyewitness accounts and geological reconstructions [*Verbeek*, 1885; *Carey et al.*, 1996], a climactic pyroclastic flow seems to have had lighter components of the flow than water, which could travel over the sea surface when the flow encountered the sea, as suggested by geological and historical examples [e.g., *Cas and Wright*, 1991; *Fisher et al.*, 1993; *Allen and Cas*, 2001; *Edmonds and Herd*, 2005; *Maeno and Taniguchi*, 2007]. A laboratory experiment suggests that even if the flow density is lighter than water the flow may trigger the large water wave in cases with a low density contrast between the flow and water [*Monaghan et al.*, 1999]. In previous studies of the Krakatau tsunami, however, the effect of such lighter components of pyroclastic flow than seawater remained ambiguous [*Nomanbhoy and Satake*, 1995; *De Lange et al.*, 2001].

[8] The lateral-blast hypothesis was also proposed on the basis of observations of the blast event that occurred during the Mount St. Helens eruption in 1980 [*Camus and Vincent*, 1983]; however, this hypothesis is now considered unacceptable because lateral blasts are inefficient for the displacement of water and the St. Helens event is thought to be caused by the emplacement of debris flow [*Francis*, 1985]. A lateral blast should also be highly directional; therefore, it is not expected to produce a uniform distribution of wave heights as observed for the Krakatau eruption, and then the deposits produced by a lateral blast should consist mainly of lithic fragments derived from the old Rakata Island [e.g., *De Lange et al.*, 2001].

[9] The Krakatau tsunamis were detected at significant distances from the source in the Indian, Atlantic, and Pacific Oceans, but it is difficult to explain these transoceanic tsunamis by direct propagation from the Krakatau Islands [*Choi et al.*, 2003]. Instead, air waves, which might couple with sea waves, are thought to be a potential generation mechanism for tsunamis observed at very distant locations [e.g., *Ewing and Press*, 1955].

[10] In this paper, we investigate tsunami generation and the propagation processes of the 1883 Krakatau eruption and constrain source parameters based on numerical simulations and existing observations for the region around Sunda Strait. First, the pyroclastic flow hypothesis is investigated, where we examine the physical process of the flow entering the sea and generating a tsunami using two-layer shallow water models. We use two types of two-layer shallow water models, dense- and light-type models, to evaluate the effect of flow density. The models describe the kinetic and dynamic interactions between density currents and seawater. Previous studies have not considered such detailed physical processes [e.g., *Nomanbhoy and Satake*, 1995]. Second, a caldera collapse hypothesis is examined using a simple plunger model, which is used in the numerical simulation of tsunamis gener-

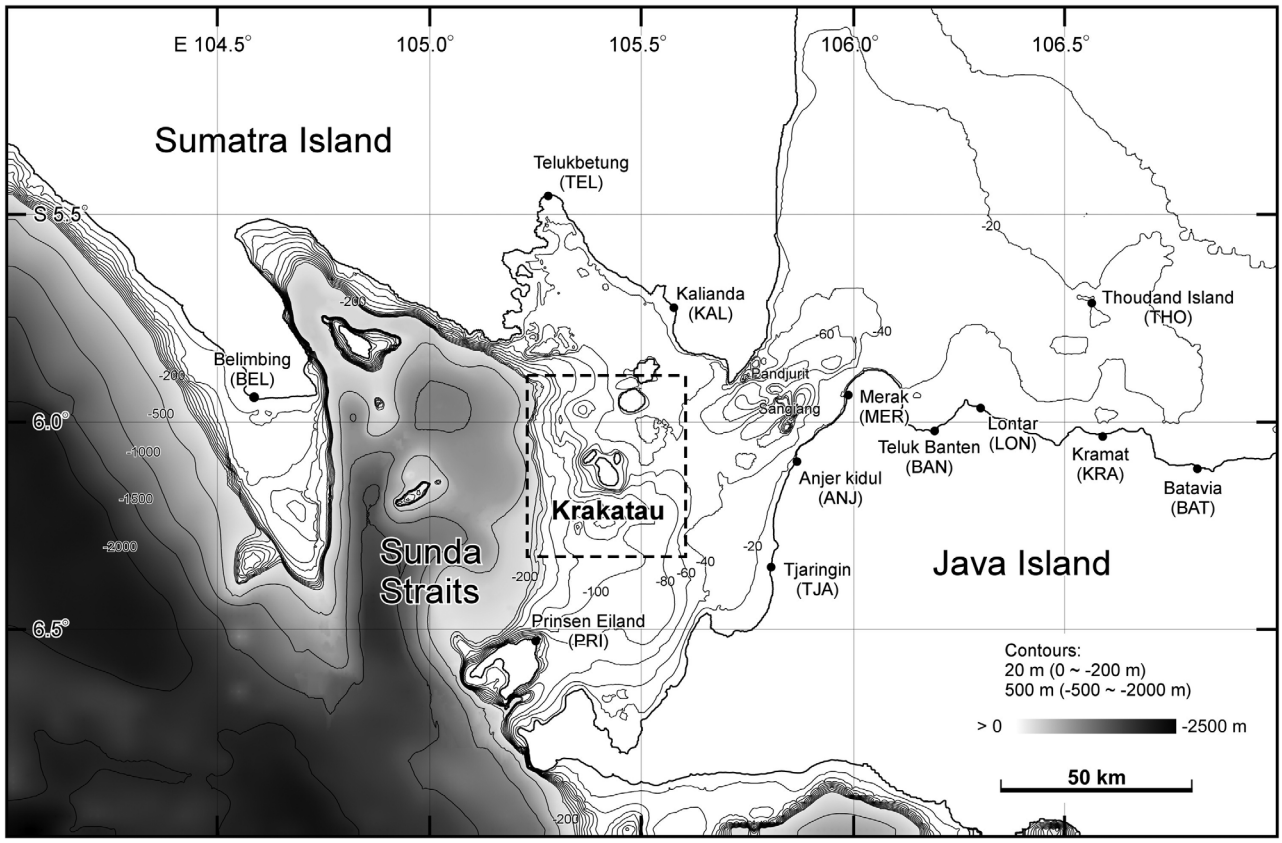

Figure 1. A map of Sunda Strait, Indonesia, and the location of the Krakatau Islands. Numerical tsunami simulation data were compared with observations at 12 locations (circles). The proximal area surrounded by a dashed line has an 83.33 m mesh (Zone A). This is combined with a distal area with a 250 m mesh (Zone B).

ated by a caldera collapse [*Maeno et al.*, 2006]. Third, a single phreatomagmatic explosion hypothesis is examined, in which simple empirical models for underwater explosions in shallow water [*Le Mehaute and Wang*, 1996] are used, as this is a concept that has not been examined thoroughly enough; the results should be helpful in constraining potential tsunami generation mechanisms during such an eruption. Finally, numerical results from each hypothesis are compared with observations at locations along the coasts of the Sunda Strait (Figure 1), and the validity of each model is discussed based on trustworthy tsunami data that were measured and estimated immediately after the eruption, including the Batavia tidal gauge record [*Verbeek*, 1885; *Symons*, 1888; *Simkin and Fiske*, 1983].

2. Timing of Tsunamis and Pyroclastic Flows During the 1883 Krakatau Eruption

[11] A climactic explosive event of the 1883 Krakatau eruption began on the afternoon of 26 August 1883, following numerous small phreatic and phreatomagmatic eruptions that began on 20 May 1883. The events of 26 to 27 August were characterized by successive small eruptions accompanied by small pyroclastic flows and tsunamis and four large explosions that occurred at 05:30, 06:44, 10:02 and 10:52 (local time) on 27 August [*Symons*, 1888; *Self and Rampino*, 1981]. The most intense explosion is thought to have occurred at 10:02 on 27 August, based on an atmospheric pressure change detected at 10:15 at Batavia, present-day Jakarta, on the northern coast of Java [*Simkin and Fiske*, 1983]. Immediately after this climactic explosion, coastal areas around the Krakatau Islands were hit by the devastating tsunami. On the coast of Batavia, this tsunami was recorded at a tide-gauge station with a wave height of at least 1.8 m at 12:36 (Batavia local time). Accurate timing of the generation of the tsunami and pyroclastic flow associated with the climactic activity is difficult to establish, but it is likely that they coincided closely with the 10:02 explosion. A collapse of the caldera also occurred during or after this explosive phase, resulting in the disappearance of the old volcanic edifice of Rakata Island (see Figure 2). The eruption continued after the most intense phase, but gradually declined [*Self and Rampino*, 1981; *Simkin and Fiske*, 1983].

[12] Tsunami runup heights were measured after the eruption along the coasts of Java and Sumatra [*Verbeek*, 1885]. Along the coasts of Java and small islands close to the narrowest part of Sunda Strait (e.g., Anjer kidur, Merak, Pandjurit, Sangiang), the tsunami runup heights reached 30 to 40 m [*Verbeek*, 1885; *Simkin and Fiske*, 1983]. Afterwards, tsunami wave heights were estimated to be about 15 m for many locations along Sunda Strait [*Symons*, 1888]. Shallow marine

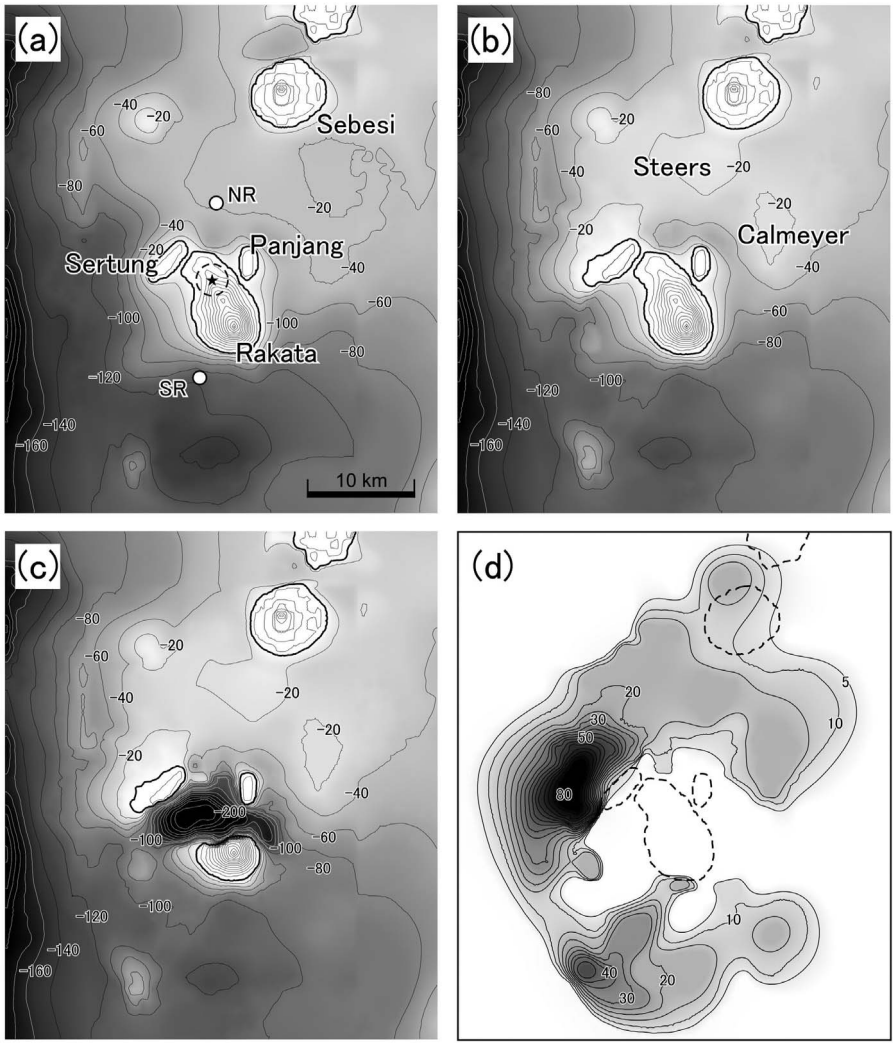

Figure 2. Maps of the Krakatau Islands and the surrounding area before and after the 1883 eruption that were reproduced by digitizing original bathymetrical data [*Simkin and Fiske*, 1983; *Sigurdsson et al.*, 1991]. Bathymetry and topography of (a) before pyroclastic flow deposition and before caldera collapse; (b) after pyroclastic flow deposition but before caldera collapse; (c) after pyroclastic flow deposition and after caldera collapse. (d) Difference between Figures 2b and 2a, showing the variation in thickness of the pyroclastic flow deposit. Figure 2a was used for the pyroclastic flow model; Figures 2b and 2c were used for the caldera collapse model; Figure 2c was used for the phreatomagmatic explosion model. SR and NR in Figure 2a indicate near-field locations where numerical simulation data are obtained.

tsunami deposits, consisting of sandy layers with abundant reworked shell and carbonate fragments, were also formed at Teluk Banten, to the north of Java [*van den Bergh et al.*, 2003].

[13] The bathymetry around the Krakatau Islands was dramatically changed by the deposition of a large amount of volcanic material, most of which originated from four intense explosions on 27 August [*Self and Rampino*, 1981; *Carey et al.*, 1996; *Mandeville et al.*, 1996]. The ignimbrite was emplaced mainly to the northwest on a shallow marine shelf with a mean water depth around 40 m within a 15 km radius of the volcano [*Sigurdsson et al.*, 1991] (Figure 2). Several flow units were deposited proximally [*Carey et al.*, 1996]. *Mandeville et al.* [1996] showed that the submarine ignimbrite is identical to the subaerial facies based on granulometry. Moreover lithic clasts from core samples retrieved at a distance of 10 km from the caldera center in 20 m water depth gave an emplacement temperature of about 500°C using the thermal remanent magnetism method [*Mandeville et al.*, 1994], indicating that the flow was a hot pyroclastic flow that could enter the sea and travel at least this distance while maintaining high temperatures. The flows entered the sea and deposited hot massive ignimbrite on the seafloor at a present water depth of about 40 m. One remarkable observation is that the pyroclastic flows largely bypassed the annular moat of relatively deep basins surrounding the source

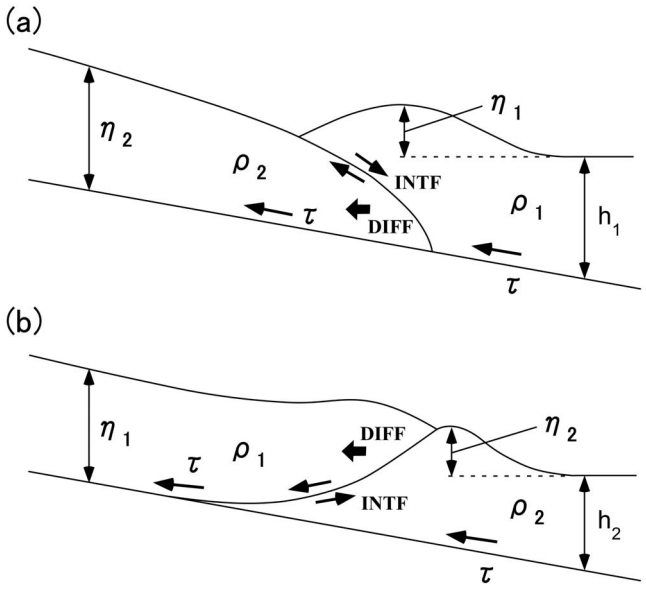

Figure 3. Two-types of two-layer shallow water models, describing pyroclastic flows entering the sea. (a) Dense-type model (DPF), where η_1 is the water surface elevation, η_2 is the thickness of a dense flow, and h_1 is the still water depth; (b) light-type model (LPF), where η_1 is the thickness of a light flow, η_2 is the water surface elevation, and h_2 is the still water depth. For both models, ρ is the density of flow or water, τ is the bottom friction, *INTF* is the interfacial shear stress, and *DIFF* is the turbulent diffusion force.

and deposited only farther out. It is therefore possible that the flows were not denser than seawater when they entered the sea and did not pond in these basins, as suggested by a theoretical and experimental study [*Legros and Druitt*, 2000]. On the other hand, much lighter components of pyroclastic flows traveled over the sea surface for over 60 km like pyroclastic surges and some of the lobes reached the northern islands of Sebesi and Sebeku, and hit the coastal area of Sumatra [*Simkin and Fiske*, 1983; *Carey et al.*, 1996, 2000]. Some of the death toll resulted from this hot less-dense component of the pyroclastic flows; however, most of victims were killed as a result of the huge tsunami.

3. Reconstruction of Bathymetry Around the Krakatau Islands

[14] The topography and bathymetry of the Krakatau Islands and the surrounding region (about 25 km from the source) before and after the 1883 eruption were reconstructed by digitizing printed maps and figures [*Simkin and Fiske*, 1983; *Sigurdsson et al.*, 1991] (Figure 2). For the more distal areas, we obtained topographic and bathymetric data by digitizing printed maps [*U.S. Army Map Service*, 1954] and utilizing ETOPO1 [*Amante and Eakins*, 2009] with GEODAS, Geophysical Data System, managed by the U.S. NGDC/NOAA (National Geophysical Data Center of the National Oceanic and Atmospheric Administration). These data were then combined and interpolated with data from more proximal areas (Figures 1 and 2). Using these data, we made original maps sampled by an 83.33 m (= 250/3 m) grid for the proximal area (Zone A) and a 250 m grid for the distal area (Zone B). In the numerical simulations, a continuation-of-regions procedure was used to combine the two zones.

4. Modeling the Tsunami Generation Process

4.1. A Numerical Model of Tsunami

[15] For all three models (pyroclastic flow entering sea, caldera collapse, and phreatomagmatic explosion), the following two dimensional nonlinear shallow water wave equations [*Goto et al.*, 1997] are used to calculate tsunamis in Zones A and B, excepting in cases where flow-water interactions occur:

$$\frac{\partial \eta}{\partial t}+\frac{\partial M}{\partial x}+\frac{\partial N}{\partial y}=0 \tag{1}$$

$$\frac{\partial M}{\partial t}+\frac{\partial}{\partial x}\left(\frac{M^2}{D}\right)+\frac{\partial}{\partial y}\left(\frac{MN}{D}\right)+gD\frac{\partial \eta}{\partial x}+\frac{\tau_x}{\rho}=0 \tag{2}$$

$$\frac{\partial N}{\partial t}+\frac{\partial}{\partial y}\left(\frac{N^2}{D}\right)+\frac{\partial}{\partial x}\left(\frac{MN}{D}\right)+gD\frac{\partial \eta}{\partial y}+\frac{\tau_y}{\rho}=0 \tag{3}$$

$$\frac{\tau_x}{\rho}=\frac{gn_m^2}{D^{\frac{7}{3}}}M\sqrt{M^2+N^2} \tag{4}$$

$$\frac{\tau_y}{\rho}=\frac{gn_m^2}{D^{\frac{7}{3}}}N\sqrt{M^2+N^2} \tag{5}$$

where η is the water surface elevation, h is the still water depth, $D = h + \eta$ is the total depth, M and N are the discharge in the x and y directions, ρ is the density of water, g is the gravitational acceleration, τ/ρ is the bottom friction term, and n_m is the Manning coefficient (= 0.025). To numerically solve these systems, we used a finite difference method with a leapfrog scheme and a second-order truncation error, and the CFL condition, which is generally used in numerical simulations of shallow water waves [e.g., *Goto et al.*, 1997]. Artificial viscosities were introduced into the mass conservation equation to control numerical instability and avoid numerical dissipations near the source. This is described as $\beta\Delta x^3(\sqrt{g/D})\|\partial^2\eta/\partial x^2\|(\partial^2\eta/\partial x^2)$ [*Goto and Shuto*, 1983], where β is a constant and set to be 1.2.

4.2. Models of Pyroclastic Flows Entering the Sea

[16] To calculate pyroclastic flows and tsunamis simultaneously, two types of two-layer shallow water models, a dense-type (DPF) model and a light-type (LPF) model, are used (Figures 3a and 3b). Both models are based on a shallow water theory and two-dimensional Euler equations. They are solved by integrating Euler equations of mass and momentum continuity in each layer, with kinetic and dynamic conditions at the free surface and interfaces. The models assume a hydrostatic pressure distribution and negligible interfacial mixing [*Imamura and Imteaz*, 1995]. Although a density change by particle sedimentation can eventually be signifi-

cant with time, our models assume a uniform density and velocity distribution during the initial phase of interaction with seawater. The two-layer models are used in the near-field (Zone A), and a single-layer shallow water model, equations (1)–(5), is used in the far-field (Zone B) (Figure 1).

[17] A dense-type two-layer shallow water model is used for a pyroclastic flow that is denser than seawater. In this case, relatively dense pyroclasts are assumed to be the dominant components of the flow, which can therefore intrude into seawater as it travels along the slope (Figure 3a). A light-type two-layer shallow water model is used for a pyroclastic flow that is lighter than seawater (Figure 3b). In this case, light pumice and ash are assumed to be the dominant components of the flow, and they thus travel over the sea surface. Laboratory experiments suggest that a low density contrast between the flow and seawater is effective to generate water waves even if the flow density is lighter than water [*Monaghan et al.*, 1999]. A lighter component of the climactic pyroclastic flow could travel over the sea surface for over 60 km and reach the south coast of Sumatra [*Verbeek*, 1885; *Carey et al.*, 1996, 2000], but here we do not focus on this type of far-reaching dilute flow that mainly consists of gas and fine-ash and is probably produced by segregation of dense particles from the main part of the flow. The effect of dilute components of pyroclastic flows on the sea surface has been considered in other studies [*Tinti et al.*, 2003; *Watts and Waythomas*, 2003; *Dufek and Bergantz*, 2007; *Dufek et al.*, 2007]. Here we consider a less dense flow such as a gravity intrusion [e.g., *De Rooij et al.*, 1999; *McLeod et al.*, 1999; *Legros and Druitt*, 2000] that has a density close to that of seawater. This type of flow may appear in the initial phase of pyroclastic flows entering the sea, particularly in proximal portions, and it will contribute more than far-reaching dilute flows to tsunami generation.

[18] The former model has been developed and improved by laboratory experiments and theoretical studies [*Imamura and Imteaz*, 1995; *Matsumoto et al.*, 1998; *Kawamata et al.*, 2005], and applied to actual examples of volcanic landslides and pyroclastic flows [e.g., *Kawamata et al.*, 2005; *Maeno and Imamura*, 2007]. The governing equations include full nonlinearity under the assumption of a long wave approximation. Subscripts 1 and 2 indicate the upper water layer and the lower dense flow layer, respectively. Equations for the upper layer are

$$\frac{\partial(\eta_1-\eta_2)}{\partial t}+\frac{\partial M_1}{\partial x}+\frac{\partial N_1}{\partial y}=0 \tag{6}$$

$$\frac{\partial M_1}{\partial t}+\frac{\partial}{\partial x}\left(\frac{M_1^2}{D_1}\right)+\frac{\partial}{\partial y}\left(\frac{M_1N_1}{D_1}\right)+gD_1\frac{\partial \eta_1}{\partial x}+\frac{\tau_x}{\rho_1}-INTF_x=0 \tag{7}$$

$$\frac{\partial N_1}{\partial t}+\frac{\partial}{\partial y}\left(\frac{N_1^2}{D_1}\right)+\frac{\partial}{\partial x}\left(\frac{M_1N_1}{D_1}\right)+gD_1\frac{\partial \eta_1}{\partial y}+\frac{\tau_y}{\rho_1}-INTF_y=0 \tag{8}$$

and those for the lower layer of a dense-type model are

$$\frac{\partial \eta_2}{\partial t}+\frac{\partial M_2}{\partial x}+\frac{\partial N_2}{\partial y}=0 \tag{9}$$

$$\frac{\partial M_2}{\partial t}+\frac{\partial}{\partial x}\left(\frac{M_2^2}{D_2}\right)+\frac{\partial}{\partial y}\left(\frac{M_2N_2}{D_2}\right)+gD_2\left(\alpha\frac{\partial D_1}{\partial x}+\frac{\partial \eta_2}{\partial x}-\frac{\partial h_1}{\partial x}\right)+\frac{\tau_x}{\rho_2}+\alpha INTF_x=DIFF_x \tag{10}$$

$$\frac{\partial N_2}{\partial t}+\frac{\partial}{\partial y}\left(\frac{N_2^2}{D_2}\right)+\frac{\partial}{\partial y}\left(\frac{M_2N_2}{D_2}\right)+gD_2\left(\alpha\frac{\partial D_1}{\partial y}+\frac{\partial \eta_2}{\partial y}-\frac{\partial h_1}{\partial y}\right)+\frac{\tau_y}{\rho_2}+\alpha INTF_y=DIFF_y \tag{11}$$

where η_1 is the water surface elevation, η_2 is the thickness of a dense flow, h is the still water depth, $D_1 = h + \eta$ is the total depth, for a dense pyroclastic flow $D_2 = \eta_2$, M and N are the discharge in the x and y directions, respectively, ρ is the density of water or flow, α is the density ratio ($= \rho_1/\rho_2$), τ/ρ is the bottom friction term, *INTF* is the term of interfacial shear stress, and *DIFF* is the term of turbulent diffusion force.

[19] Stress terms (bottom friction, interfacial shear stress and turbulent diffusion stress) for the x and y directions are given as the following equations (the same for both dense- and light- type models):

$$\frac{\tau_x}{\rho}=\frac{gn_b^2}{D^{\frac{7}{3}}}M\sqrt{M^2+N^2} \tag{12}$$

$$\frac{\tau_y}{\rho}=\frac{gn_b^2}{D^{\frac{7}{3}}}N\sqrt{M^2+N^2} \tag{13}$$

$$INTF_x=f\bar{u}\sqrt{\bar{u}^2+\bar{v}^2} \tag{14}$$

$$INTF_y=f\bar{v}\sqrt{\bar{u}^2+\bar{v}^2} \tag{15}$$

$$DIFF_x=k\sqrt{\frac{\partial^2 M}{\partial x^2}+\frac{\partial^2 M}{\partial y^2}} \tag{16}$$

$$DIFF_y=k\sqrt{\frac{\partial^2 N}{\partial x^2}+\frac{\partial^2 N}{\partial y^2}} \tag{17}$$

where n_b is the bottom friction coefficient, f is the interfacial drag coefficient between the density current and water, $\bar{u}$ and $\bar{v}$ are the relative velocities between flow and water in the x and y directions, respectively, and k is the turbulent diffusion coefficient. For the water layer, n_b is equivalent to the Manning coefficient, n_m (= 0.025).

[20] Another model is a modified version of the existing two-layer shallow water model. Its fundamental physics and governing equations are similar to the dense-type model, and the order of layers is switched. Subscripts 1 and 2 indicate the upper light pyroclastic flow layer and the lower water layer, respectively. Equations for the upper layer are given as

$$\frac{\partial \eta_1}{\partial t}+\frac{\partial M_1}{\partial x}+\frac{\partial N_1}{\partial y}=0 \tag{18}$$

$$\frac{\partial M_1}{\partial t}+\frac{\partial}{\partial x}\left(\frac{M_1^2}{D_1}\right)+\frac{\partial}{\partial y}\left(\frac{M_1N_1}{D_1}\right)+gD_1\left(\frac{\partial \eta_1}{\partial x}+\frac{\partial \eta_2}{\partial x}\right)+INTF_x = DIFF_x \tag{19}$$

$$\frac{\partial N_1}{\partial t}+\frac{\partial}{\partial y}\left(\frac{N_1^2}{D_1}\right)+\frac{\partial}{\partial x}\left(\frac{M_1N_1}{D_1}\right)+gD_1\left(\frac{\partial \eta_1}{\partial y}+\frac{\partial \eta_2}{\partial y}\right)+INTF_y = DIFF_y \tag{20}$$

and those for the lower layer of a light-type mode are given as

$$\frac{\partial \eta_2}{\partial t}+\frac{\partial M_2}{\partial x}+\frac{\partial N_2}{\partial y}=0 \tag{21}$$

$$\frac{\partial M_2}{\partial t}+\frac{\partial}{\partial x}\left(\frac{M_2^2}{D_2}\right)+\frac{\partial}{\partial y}\left(\frac{M_2N_2}{D_2}\right)+gD_2\left(\alpha\frac{\partial \eta_1}{\partial x}+\frac{\partial \eta_2}{\partial x}\right)+\frac{\tau_x}{\rho_2}-\alpha INTF_x=0 \tag{22}$$

$$\frac{\partial N_2}{\partial t}+\frac{\partial}{\partial y}\left(\frac{N_2^2}{D_2}\right)+\frac{\partial}{\partial y}\left(\frac{M_2N_2}{D_2}\right)+gD_2\left(\alpha\frac{\partial \eta_1}{\partial y}+\frac{\partial \eta_2}{\partial y}\right)+\frac{\tau_y}{\rho_2}-\alpha INTF_y=0 \tag{23}$$

where η_1 is the thickness of a light pyroclastic flow, η_2 is the water surface elevation, h is the still water depth, $D_2 = h + \eta$ is the total depth, for a dense pyroclastic flow $D_1 = \eta_1$, and the definitions of the other parameters and the terms are the same as for the dense-type model above.

[21] The drag forces between each layer are incorporated with kinetic interactions between flow and water. In previous studies where laboratory experiments were compared to numerical simulations using a two-layer shallow water model [*Matsumoto et al.*, 1998; *Kawamata et al.*, 2005], the bottom friction coefficient was set to be 0.01 for subaerial flow (n_a) and 0.12 for underwater flow (n_w) to reproduce the behaviors of experimental flows and water waves. However, the numerical results using these values do not necessarily agree with the time-distance relationship when less dense particulate gravity currents flow into water [e.g., *McLeod et al.*, 1999]. This is probably because turbulent suspension is more important in sustaining less dense particulate currents than grain-grain interaction in dense granular flows. For the pyroclastic flows of the Krakatau eruption, we suppose that the flows were rich in gas and as a result, turbulent suspension was effective and enabled the relatively low-density pyroclastic flows to travel over or under the sea.

[22] To obtain the relationship between time, t, and distance, x, of density currents described as a form of $x \propto t^{2/3}$, which is determined by laboratory experimental results [e.g., *McLeod et al.*, 1999], the bottom friction coefficient, n_b, for both dense- and light-type flow models is set to be 0.01 to 0.06 for on-land conditions (n_a) and 0.06 to 0.08 for underwater conditions (n_w). The interfacial drag coefficients, f, between the pyroclastic flow and seawater were set to be 0.06 to 0.2. The value of 0.2 was determined through laboratory experiments [*Matsumoto et al.*, 1998; *Kawamata et al.*, 2005]. For both dense- and light- type models, k is assumed to be equivalent to the coefficient of eddy viscosity. The contribution from kinematic viscosity is negligible because its effect is much smaller than the eddy viscosity in pyroclastic flows [e.g., *Takahashi and Tsujimoto*, 2000]. For the coefficient of eddy viscosity $\kappa Du/6$ is used [*Lane and Kalinske*, 1941; *Takahashi and Tsujimoto*, 2000], where κ is the von-Karman constant (= 0.4), u is the velocity of the pyroclastic flow and equivalent to $\sqrt{gD}\sin\theta$, and θ is the slope angle.

[23] A time step Δt was initially set to be 0.05 s (while pyroclastic flows entered the sea), then after 40 min was changed to 0.2 s to avoid numerical dissipation. The duration of all simulations was 6 h. Artificial viscosities were introduced into the mass conservation equation to control numerical instability.

4.3. Initial Conditions of the Pyroclastic Flow

[24] The total volume of pyroclastic flows from the 1883 Krakatau eruption is estimated based on the submarine tephra volume of 21.6 km^3 (9.7 km^3 DRE, Dense Rock Equivalence) plus 0.8 km^3 (0.4 km^3 DRE) of subaerial pyroclastic flow deposits [*Carey et al.*, 1996; *Mandeville et al.*, 1996]. *Sigurdsson et al.* [1991] suggested that a volume of 6.5 km^3 (DRE) was deposited as ignimbrite in the ocean within a 15 km radius of the volcano. Although the ignimbrite associated with four flow units was thought to correspond to the products from four intense explosions [*Self and Rampino*, 1981; *Carey et al.*, 1996], the accurate volumes of deposits for each event are difficult to establish. We therefore assume a total volume (V) of 5, 10 or 20 km^3 (2.5, 5 or 10 km^3 in DRE assuming a density of about 1200 kg/m^3) for the pyroclastic flow produced during the most intense activity around 10:00 on 27 August. The source was located in the north of the old Rakata Island (Figure 2a), based on geological insight and eyewitness accounts [*Simkin and Fiske*, 1983].

[25] In our numerical simulation, pyroclastic flows were erupted with a volume flux, Q, prescribed as

$$Q = Q_{\max}\sin\left(\frac{t\pi}{T}\right) \tag{24}$$

where $Q_{\max}$ is the maximum volume flux, t is the time from the beginning of pyroclastic flow eruption, and T is the duration of the eruption, assuming waning and waxing phases (Figure 4), and from a circular source with a diameter of 2 or 3 km (in most cases set to be 2 km). Using a total volume of pyroclastic flows, an average volume flux, Q_{ave}, can be simply written as V/T. $Q_{\max}$ is described as $\pi Q_{ave}/2$. An initial flow thickness, h_i, at the circular source is changed with the following function:

$$\frac{dh_i}{dt}=\frac{Q}{\pi(d/2)^2} \tag{25}$$

where d is the diameter of a circular source. The flow had a vertical flux at first, then gravitationally collapsed and spread radially along the topography. The lateral flux took on the same order as the initial vertical one (Figure 4).

[26] The bulk flow density was assumed to be 900 to 1500 kg/m^3, which is generally accepted as the density of pyroclastic flows [e.g., *Druitt*, 1997]. Based on the theo-

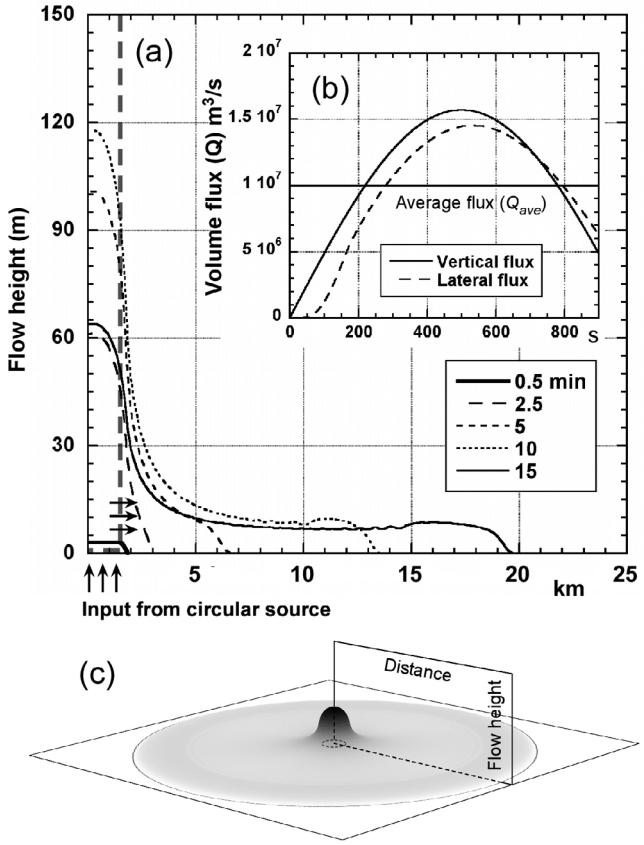

Figure 4. A representative initial condition of pyroclastic flow generation from a circular source. (a) Time profiles of a dense flow layer on a horizontal plane under the condition of the density of 1100 kg/m^3 with the volume of 10 km^3 and the average flux of 10^7 m^3/s (model DPF10–7La in Table 1). Input flux is controlled following a sine function. Duration of the eruption (T) is 1000 s. (b) Initial lateral flux balances with vertical flux where an x-axis is seconds. (c) A schematic representation of a flow.

retical and experimental studies of *Legros and Druitt* [2000] where the mechanism of flows temporarily pushing back the shoreline was investigated, a density of 900 to 1100 kg/m^3 may be more plausible for the pyroclastic flows of the 1883 Krakatau eruption. Here we assumed 1100 to 1500 kg/m^3 for dense-type model and 900 to 1000 kg/m^3 for light-type model. These density values are also consistent with sedimentological data obtained by piston cores, in which the average density of pumiceous pyroclastic deposits is measured to be about 1000 kg/m^3 [*Mandeville et al.*, 1996]. An average volume flux was assumed to be 10^6 to 10^8 m^3/s, corresponding to the possible range of discharge rates for VEI 6 to 7 class caldera-forming eruptions [e.g., *Wilson et al.*, 1980; *Bursik and Woods*, 1996]. Parameter studies were conducted under the ranges of these physical values for pyroclastic flows (Table 1).

4.4. Model of a Caldera Collapse and Tsunami Generation

[27] To investigate tsunamis generated by caldera collapse, a simple piston-like plunger model is used combining with a single layer shallow water model, equations (1)–(5). The model assumes that the topographic height of the collapsing area linearly decreases with time as a change from topography before collapse (Figure 2b) to one after collapse (Figure 2c). This method was applied to examine tsunamis during a caldera formation at Kikai caldera in Japan [*Maeno et al.*, 2006]. In the governing equations, η in equation (1) is replaced with $\eta - h$, where h corresponds to the topographic height that changes with time. The duration of caldera collapse has not been well constrained. In the cases of the collapsing Kikai caldera, rapid collapse conditions with a duration of a few to a few tens of minutes were able to generate the largest tsunamis; however the most plausible collapse duration was estimated to be longer than several hours [*Maeno et al.*, 2006; *Maeno and Imamura*, 2007]. Here, we select a caldera collapse duration (T_c) of 1, 5, 10, 30 min and 1 h to acquire typical tsunami wave characteristics. A caldera collapse speed, V_c, and a dimensionless caldera collapse speed, V_c*, can also be defined using a maximum topographic change and a water velocity flowing into the caldera (Table 2). The time step Δt

Table 1. Initial Conditions of Numerical Simulations of Tsunamis Generated by Pyroclastic Flows Entering the Sea[a]

Model	V	Q_{ave}	ρ	d	n_a	n_w	f
DPF05–6L	5	1.E+06	1100	3	0.01	0.08	0.20
DPF05–6H	5	1.E+06	1500	3	0.01	0.08	0.20
DPF05–7L	5	1.E+07	1100	3	0.01	0.08	0.20
DPF05–7H	5	1.E+07	1500	3	0.01	0.08	0.20
DPF05–8L	5	1.E+08	1100	3	0.01	0.08	0.20
DPF05–8H	5	1.E+08	1500	3	0.01	0.08	0.20
DPF10–6L	10	1.E+06	1100	3	0.01	0.08	0.20
DPF10–6H	10	1.E+06	1500	3	0.01	0.08	0.20
LPF10–7	10	1.E+07	900	3	0.06	0.06	0.18
DPF10–7La	10	1.E+07	1100	3	0.01	0.08	0.20
DPF10–7Lb	10	1.E+07	1100	3	0.06	0.06	0.06
DPF10–7H	10	1.E+07	1500	3	0.01	0.08	0.20
LPF10–8a	10	1.E+08	900	3	0.01	0.06	0.18
LPF10–8b	10	1.E+08	900	3	0.06	0.06	0.18
DPF10–8a	10	1.E+08	1100	3	0.01	0.08	0.06
DPF10–8b	10	1.E+08	1100	3	0.06	0.06	0.18
DPF20–7	20	1.E+07	1100	3	0.01	0.08	0.20
LPF20–8a	20	1.E+08	900	3	0.06	0.06	0.06
LPF20–8b	20	1.E+08	900	2	0.06	0.06	0.18
LPF20–8M	20	1.E+08	1000	2	0.06	0.06	0.18
DPF20–8a	20	1.E+08	1100	3	0.06	0.06	0.06
DPF20–8b	20	1.E+08	1100	2	0.06	0.06	0.18

[a] V, volume of pyroclastic flow (km^3); Q_{ave}, average volume flux of pyroclastic flow (m^3/s); ρ, density of pyroclastic flow (kg/m^3); d, vent diameter (km); n_a and n_w, bottom drag coefficients for on-land and sea, respectively; f, interfacial drag coefficient.

Table 2. Initial Conditions of Numerical Simulations of Tsunamis Generated by Caldera Collapse[a]

Model	T_c	V_c*
CC01	1	0.275
CC05	5	0.055
CC10	10	0.027
CC30	30	0.009
CC60	60	0.005

[a] T_c, caldera collapse duration (minutes); V_c*, dimensionless caldera collapse speed defined by $V_c/\sqrt{gh}$.

was set to be 0.5 s, and the total duration of simulation is 6 h for all models.

4.5. Model of a Phreatomagmatic Explosion and Tsunami Generation

[28] Tsunamis generated by a large water dome were numerically investigated by *Nomanbhoy and Satake* [1995], where water was moved upward to form the same volume and shape as a caldera. In the results of this model, the sea level eventually rose and a dome-shaped source was created. Although this approximation was not based on the physical considerations of underwater explosions, an initial upward displacement of ~10 km^3 of water over a period of 5 min was indicated to reproduce the observed tsunami. This result contrasts with the idea of successive submarine explosions occurring over a 30-min period as proposed by *Yokoyama* [1987]. Here we investigate the possibility of tsunamis generated by single large-scale phreatomagmatic explosions, since no fixed ideas for initial conditions have been previously determined.

[29] If the explosion takes place in shallow water (as characterized by the equation of $d_w/W^{1/3} < 1$; d_w is a depth of explosion crater; W is explosion energy in pounds of TNT) it will necessarily become a near-surface explosion [*Le Mehaute and Khangaonkar*, 1992]. The explosion energy needed to produce a large crater like the Krakatau caldera (2 to 3 km in radius) can be estimated to be 10^{16} to 10^{17} J, using the empirical relationship between crater size and explosion energy [*Sato and Taniguchi*, 1997]. For the 1883 eruption, the value of $d_w/W^{1/3}$ is estimated at 0.2 to 0.5, using the maximum depth of the caldera. Therefore, a potential largest phreatomagmatic explosion could be associated with a shallow water wave generation process, in which the water is initially expelled upwards and outward, forming a plume and a crater with a watery rim. The time required to generate a watery rim is on the order of a second to ten seconds for the explosion energy of 10^{16} to 10^{17} J [*Le Mehaute and Wang*, 1996].

[30] The water crater produced by a near-surface explosion may even expose the seafloor of the caldera to the atmosphere. After reaching its maximum size, the water crater collapses and the water rushes inward under the influence of gravity onto the crater, analogous to a dam break problem. Taking this initial condition into account, we use a physical model based on the empirical relationship between explosion energy and initial wave height for a near-surface explosion [*Le Mehaute and Wang*, 1996]. In this model, an initial water elevation is assumed to have a crater shape with a watery rim. The size of crater is determined by a simple relationship between explosion energy (E) and the initial maximum water elevation at the watery crater rim (η_i). This is empirically described as

$$\eta_i = 0.01E^{0.64} \tag{26}$$

[31] This method was used to analyze a tsunami induced by a phreatomagmatic explosion at Karymskoye Lake ($E = 10^{12}$ J) [*Torsvik et al.*, 2010] and seems to describe its wave characteristics well. Although the applicability of this model is thought to be limited, we assume it can extrapolate to larger scale explosions. The model describes the distribution of a crater shape for an initial water elevation (η) as the following equations [*Le Mehaute and Wang*, 1996]:

$$\text{if } R_e \le r_e, \quad \eta = \eta_i \left[2\left(\frac{r_e}{R_e}\right) - 1 \right] \tag{27}$$

$$\text{if } R_e > r_e, \quad \eta = 0 \tag{28}$$

where r_e is the distance from the explosion center, and R_e is the distance of the watery rim from the explosion center. In our simulation, R_e is set to be 2 to 3.5 km based on the size of the present Krakatau caldera [*Deplus et al.*, 1995]. Then, we applied this model with an initial condition of the 1883 Krakatau eruption using topographic data after the caldera collapse and pyroclastic flow events (Figure 5). In fact, the ideal initial distribution of water elevation was somewhat limited by the irregular surfaces of the topography and bathymetry (Figure 5a). Therefore, we handled their effect on the initial crater shape using the following assumptions, where η_0 is the modified wave elevation after removing the effects of topography and bathymetry (Figure 5c). Under submarine conditions ($h \ge 0$), if the water elevation (η) is deeper than the depth of the sea ($-h$), then $\eta_0 = -h$, or if the water elevation (η) is shallower than the depth of the sea, then $\eta_0 = \eta$. Under subaerial conditions ($h < 0$), if the water elevation (η) is lower than the altitude (h), then $\eta_0 = 0$, or if the water elevation is higher than altitude, then $\eta_0 = \eta + h$. The modified initial water elevation (η_0) was used as an initial condition for the numerical simulation.

[32] Under this consideration, we calculated tsunamis using equations (1)–(5) with different initial conditions ($E = 10^{16}$ J and 10^{17} J) (Table 3). In the numerical simulations, we introduced artificial viscosity to mass conservation equations to avoid a numerical instability. As a result, our models were able to incorporate explosions with energy of about 10^{17} J, which can create a crater that is 290 m deep and, correspondingly, a maximum water elevation of 290 m (Figure 5b). The time step Δt was set to be 0.5 s, and the total duration of simulation is 6 h for all models.

5. Results of Tsunami Numerical Simulations

5.1. Pyroclastic Flow Models

[33] Representative numerical results of flow behaviors using different volumes with different average fluxes are shown in Figure 6, with 5-, 15- and 30-min snapshots after the beginning of the pyroclastic flow eruption. When the dense-type (DPF) model is used, subaerially generated flows run along the slope of Rakata Island and intrude into the sea. Then, the flows continue to spread along the sea bottom. Immediately after the flows enter the sea, sea level rapidly rises, because seawater is pushed up and dragged by the underlying flows (Figures 7a and 7c). After that, sea level gradually recovers, resulting in the generation of a large tsunami with a positive leading peak. On the other hand, when the light-type (LPF) model is used, the flows do not intrude into the sea along the seafloor. Instead, they spread out on the sea surface and push seawater away. This spreading behavior is almost the same as for the DPF models under the same initial condition (Figure 6), but has a smoother

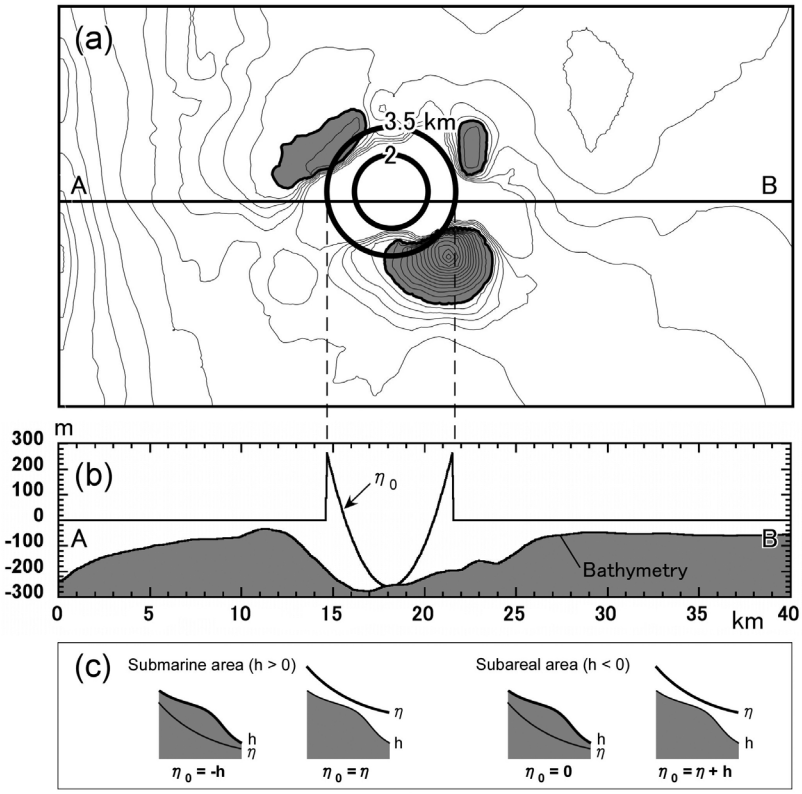

Figure 5. (a) Initial conditions of a phreatomagmatic explosion model in which crater radius of 2 or 3.5 km are used. The center of explosion crater is set at the deepest point at the current caldera. (b) A profile, along the A-B in Figure 5a, showing the initial water elevation (η_0) using a model with the explosion energy of 10^{17} J and a 3.5 km radius crater. (c) Schematic illustration of relationships between h (the still water depth) and η (the initial water elevation calculated from equation (27)) for different conditions and the definition of the modified initial water elevation (η_0) which is used in numerical simulation. See text for the detail.

interface between the flow and water than the DPF models, because of no interaction with the bathymetry. As a result, the displacement of seawater by less dense flows can also induce a tsunami with a positive leading wave (Figures 7b and 7d). For both models, seawater is rapidly pushed away and the shoreline moves offshore. This condition corresponds to the shoreline displacement observed in laboratory experiments [*Legros and Druitt*, 2000].

[34] Numerical results in distal area are shown in Figures 8a and 8b. Initially, tsunamis circularly spread from the Krakatau Islands. Afterwards, the speed and amplitude of tsunamis dramatically change depending on the bathymetry in different directions. The maximum wave height attained is about 80 m to the north of the Rakata Island when the models DPF10–8a or −8b are used. With these initial conditions, tsunami height is still over 20 m at a distance of 40 km from the source. The first positive peak arrived in 23 min at PRI (Prinsen Eiland), in 27 min at ANJ (Java) and in 28 min at KAL on the south coast of Sumatra. In Teluk Banten (BAN) and Batavia (BAT), the first positive peaks reached within 1 h and 20 min and 2 h and 30 min, respectively. On the coasts of northwest Java, the wave heights are higher than those along the coasts of Sumatra. This is probably an effect of the shallower seafloor in the northern part of the Sunda Strait. Southwest of Krakatau, the bathymetry is characterized by a very steep slope. In fact, the seafloor is more than 1000 m deep only 10 km from Krakatau. These bathymetric characteristics inevitably affect tsunami behavior in this region. A dramatic increase of sea depth (h) causes a rapid increase of tsunami velocity ($\sqrt{gh}$), and a linear wave character is likely to dominate its propagation process. For these reasons, the behavior of tsunamis in the southwestern region is much different from those in the northern region, where a strong nonlinearity appears on the wave characters. These tsunami behaviors appear in other models as well.

[35] Waveforms of tsunami with representative initial conditions of volume and flux are computed at the north and

Table 3. Initial Conditions of Numerical Simulations of Tsunamis Generated by Phreatomagmatic Explosions[a]

Model	E	η_i	R_e
PME1	5E+15	140	2
PME2	1E+16	166	2
PME3	1E+16	166	3.5
PME4	1E+17	288	3.5

[a] E, explosion energy (J); η_i, maximum initial water elevation at watery rim (m); R_e, radius of explosion crater (km).

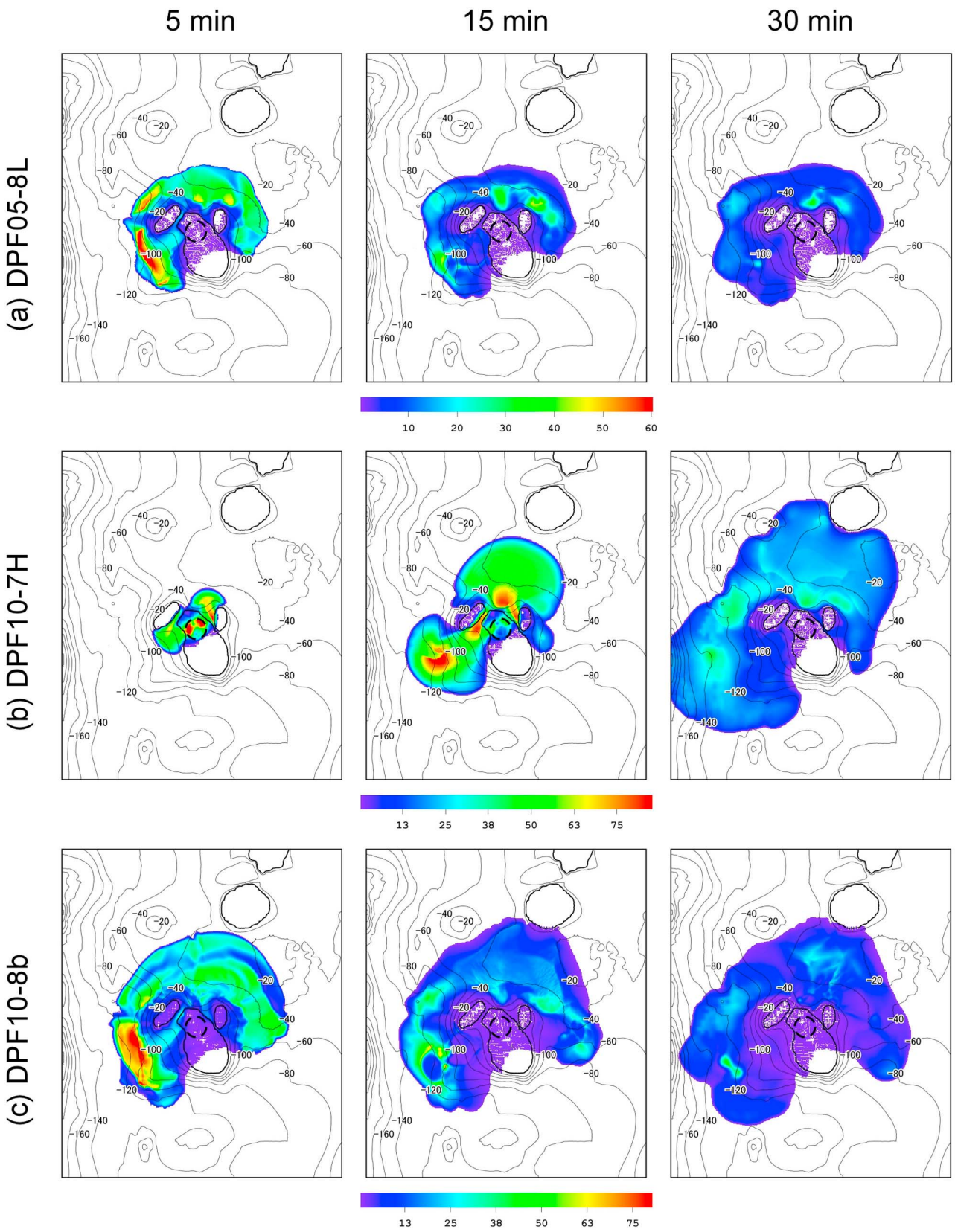

Figure 6. Numerical results of spreading behavior and thickness evolution of dense and light pyroclastic flows, using different initial conditions. Snapshots at 5, 15, and 30 min are shown for each model. Unit of color bars is meter. (a) Model DPF05–8L; (b) model DPF10–7H; (c) model DPF 10–8b; (d) model LPF10–8b; (e) model DPF20–8b; (f) model LPF20–8b. See Table 1 for the details of models.

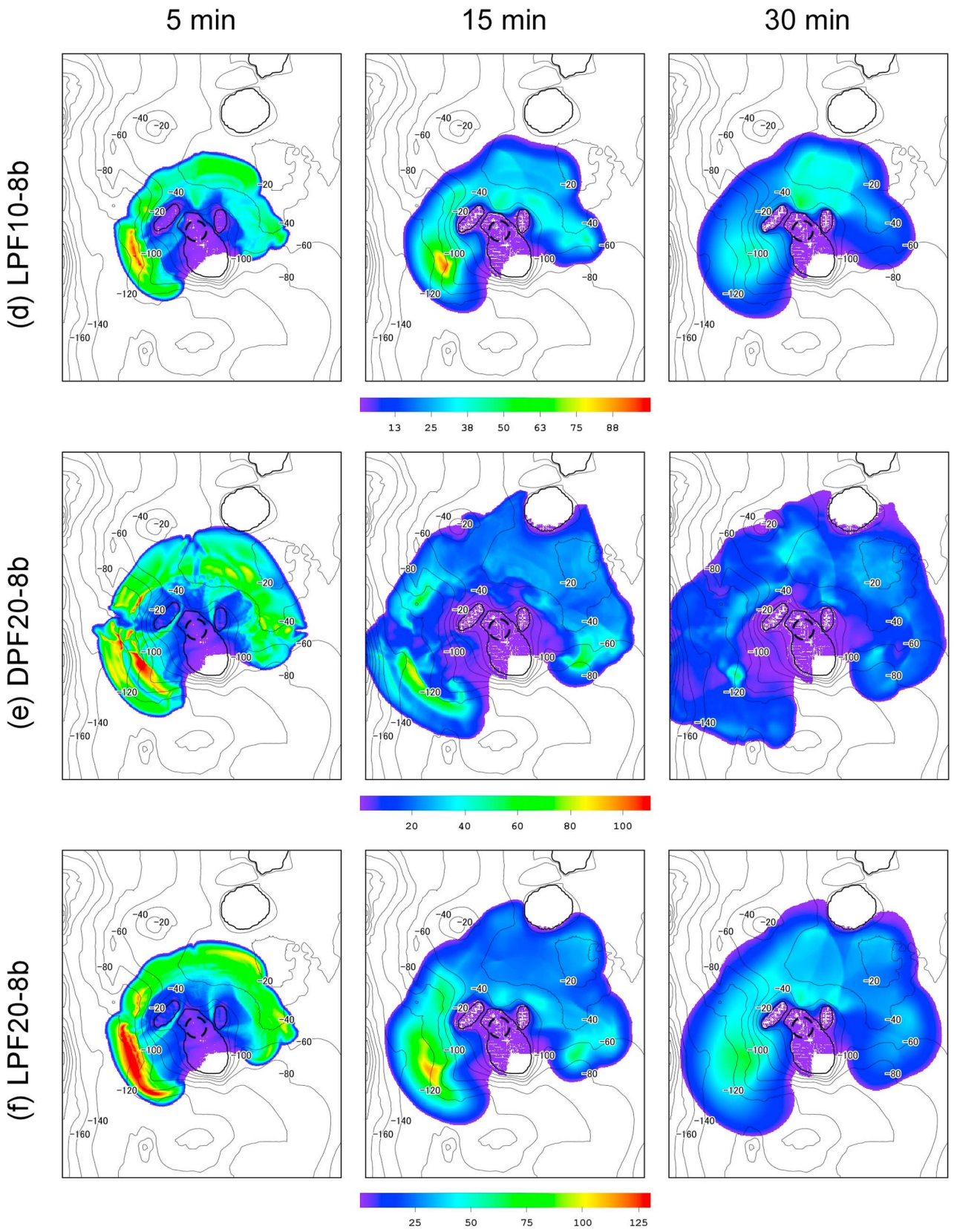

Figure 6. (continued)

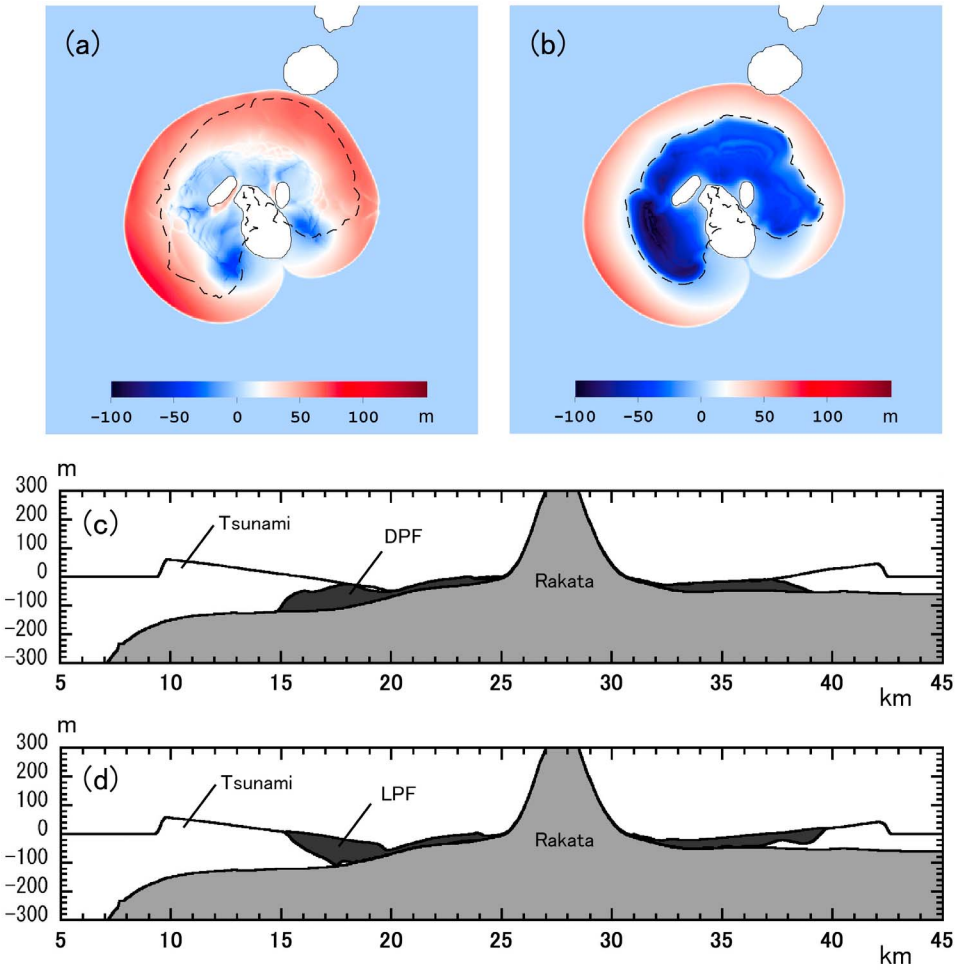

Figure 7. Numerical results of tsunami generation by pyroclastic flows entering the sea and shoreline displacement occurring around the Rakata Island at 5 min after the flow generation, using two different initial conditions. (a) Water elevation (η_1) resulted from dense-type flow model (DPF10–8b), the density of 1100 kg/m^3 with the volume of 10 km^3 and the average flux of 10^8 m^3/s, a dashed line indicates the distribution of the dense pyroclastic flow in Figure 6c. (b) Water elevation (η_2) resulted from light-type flow model (LPF10–8b), the density of 900 kg/m^3 with the volume of 20 km^3 and the average flux of 10^8 m^3/s, a dashed line indicates the distribution of the light pyroclastic flow in Figure 6d. (c and d) Cross sections (EW direction) of Figures 7a and 7b, respectively.

south of the Rakata Island (NR and SR in Figure 2a). A typical waveform is characterized by a first positive peak followed by a negative peak and having a long lasting oscillation (Figure 9). The maximum wave height of the tsunami is largest when the average volume flux is the largest. Results indicate that the wave characteristics around the caldera vary with different initial conditions—particularly with average volume flux, Q_{ave}, of the pyroclastic flows. However, the waveforms of the positive leading wave are almost all the same. In the southern part of the caldera, the initial wave amplitude becomes smaller than in the north, which is due more to the effect of topography and less to the effect of pyroclastic flows in this region. Only DPF models shown in Figure 9, but the waveform characteristics are common for LPF ones. An increase in volume, V, and density, ρ, of pyroclastic flows causes an increase in tsunami heights, but the effect of flux is much more than those of volume and density. In Figure 10, numerical results at Batavia are shown.

[36] Effects of an average volume flux of pyroclastic flow (Q_{ave}) on the initial wave amplitude of a tsunami (η) are investigated for four representative locations: the south of the Rakata Island (SR), and 2 to 3 km offshore of PRI, ANJ, and BAT (Figure 11), where DPF models are used and an average volume flux per unit width at the source ($Q'_{ave} = Q_{ave}/(\pi d)$, where d is a diameter of the source) is defined. Both flow flux (Q'_{ave}) and tsunami amplitude (η) are nondimensionalized in the following:

$$q^* = \frac{Q'_{ave}}{h_p\sqrt{gh_p}} \tag{29}$$

$$\eta^* = \frac{\eta}{h_d} \tag{30}$$

where h_p is water depth near the proximal end of the submarine flow motion, and h_d is a water depth at a distal

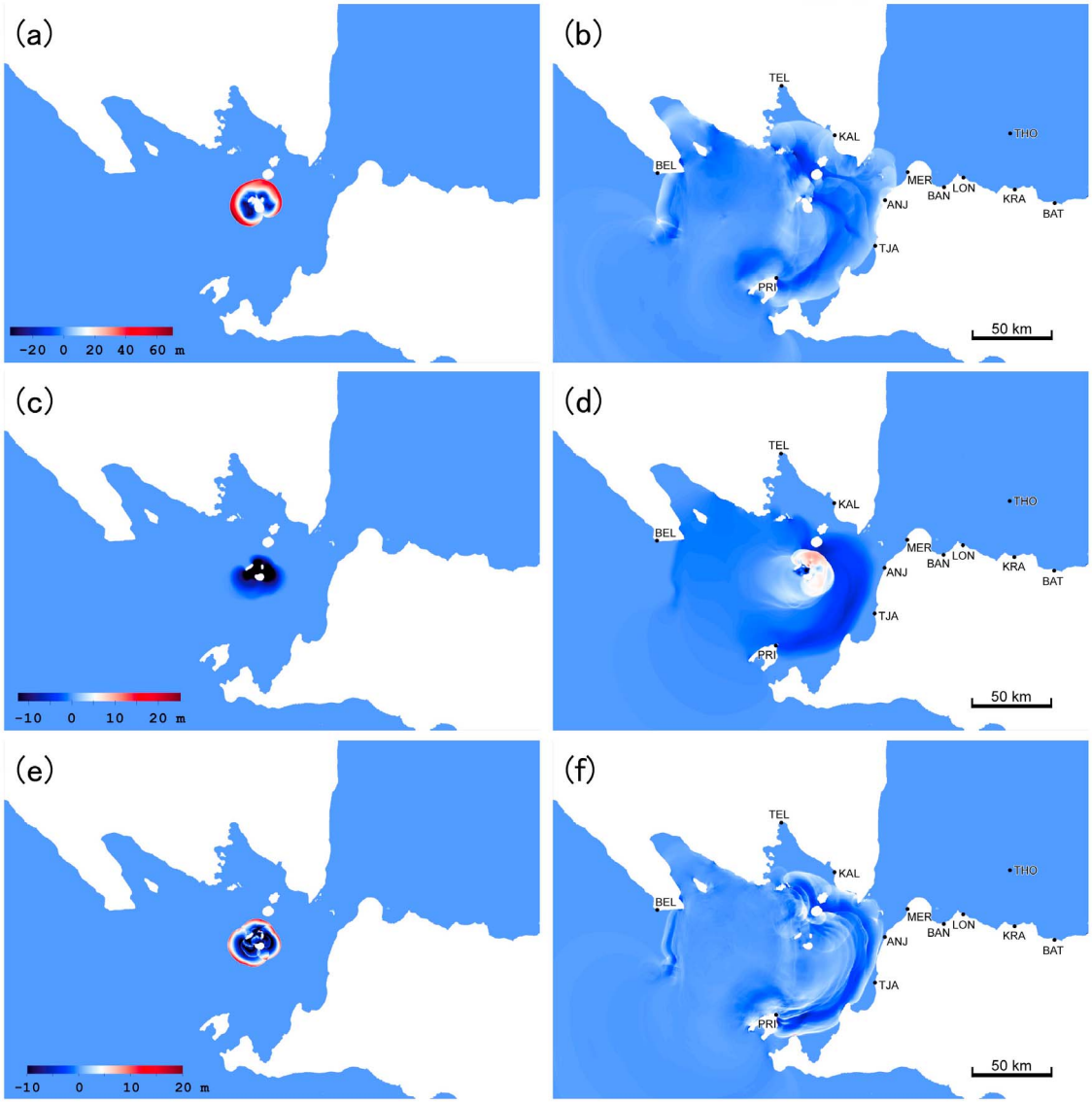

Figure 8. Results of tsunami simulations using three different models. Snapshots at 5 and 30 min are shown for each model. (a and b) Pyroclastic flow entering the sea model (DPF10–8b). (c and d) Caldera collapse model (CC05). (e and f) Phreatomagmatic explosion models (PME4).

location where wave amplitude is collected. For SR and PRI, h_p was set to be 110 m, which corresponds with a depth at SR and almost the end of submarine flow. For ANJ and BAT, it is set to be 40 m, which is the sea depth at the northeast of the caldera. A term of $h_p\sqrt{gh_p}$ means a maximum discharge of seawater when a tsunami is generated. For all four locations, η^* is observed to be strongly dependent upon q^*, as shown in Figure 11. In fact, the flow volume also affects the resultant wave amplitude, but the effect of that is less than the flux. The relationship between $1/q^*$ and η^* is approximately described by a power law as the following form:

$$\eta^* = A\left(\frac{1}{q^*}\right)^B \tag{31}$$

where A and B are regression coefficients. This simple relationship is comparable to a formulation proposed by *Walder et al.* [2003] to explain experimental data of granular flow entering water and water wave generation at near-field, in which constants A and B are determined to be 1.32 and −0.68, respectively. In our results, a value of B for the near-field (SR) becomes about −0.7 (Figure 11). This is almost the same value suggested by *Walder et al.* [2003], although some of our results obtained from higher flux models are out of an applicable range for their experimental data. It is simply obvious that there are discrepancies between our numerical results and laboratory studies, because assumptions on source conditions and flow types are different, but a detailed comparison between these studies would be interesting.

[37] Values of B in the far-field (PRI, ANJ, and BAT) become smaller than in the near-field (−0.5 for PRI and

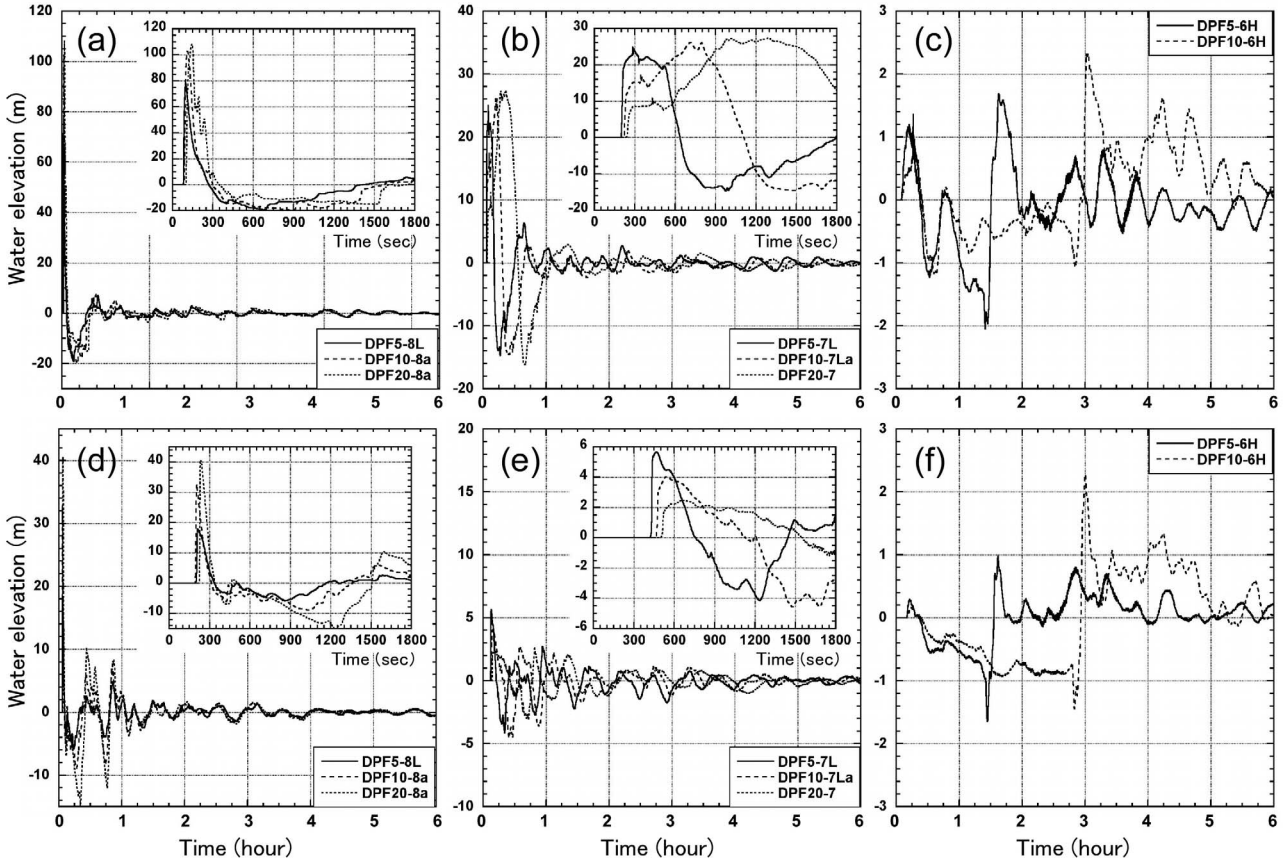

Figure 9. Computed near-field tsunami waveforms, using pyroclastic flow (DPF) models with various initial conditions. Results for the north of Rakata Island (NR) with an average volume flux of (a) 10^8 m^3/s, (b) 10^7 m^3/s, (c) 10^6 m^3/s. Results for the south of Rakata Island (SR) with an average volume flux of (d) 10^8 m^3/s, (e) 10^7 m^3/s, (f) 10^6 m^3/s. See Table 1 for the details of models. The time is from the onset of pyroclastic flow from the source. Inset figures indicate magnification of the initial phase (until 1800 s) of wave generation.

ANJ, −0.25 for BAT), where the model for the near-field seems no longer applicable. Although the physical meaning of the relationship between η^* and $1/q^*$ in our numerical results still remains unclear, it is apparent that the flow flux strongly affects wave amplitude. This tendency is consistent with experimental studies not only for dense granular flows [e.g., *Walder et al.*, 2003] but also for less dense gravity currents [e.g., *Monaghan et al.*, 1999].

5.2. Caldera Collapse Models

[38] In all caldera collapse models, immediately after collapse begins, the sea level rapidly decreases due to seawater flowing into the collapsed area. Then it eventually recovers and rises as the water wave collides and the total wave height increase. The maximum wave height (the maximum change in water elevation) of a tsunami near the caldera is achieved in the initial phase of wave generation and varies depending on the relationship between the collapse depth and velocity of seawater, as investigated on the tsunamis resulting from the Kikai caldera-forming eruption [*Maeno et al.*, 2006]. The maximum wave height is the largest when the caldera collapse duration is about 30 min (Figure 12); this corresponds to a dimensionless collapse speed ($V_c^* = V_c/\sqrt{gh}$) of 0.01. The height eventually decreases with shorter and longer collapse durations.

[39] Numerical results using model CC05 with a 5-min collapse-duration are shown in Figures 8c and 8d as an example. The first negative peak reached PRI in 24 min, ANJ in 30 min and KAL in 40 min. The first positive peak reached all locations approximately 30 to 40 min after the first negative peak. For example, at Batavia, the first negative peak arrived in 2 h 45 min, and the first positive wave in 3 h 15 min. A typical waveform shows a negative peak followed by positive leading peaks (Figure 12), which is completely opposite to the results of the pyroclastic flow models, and the arrival time of positive peaks are delayed.

5.3. Phreatomagmatic Explosion Models

[40] Numerical simulations of phreatomagmatic explosions showed that the maximum wave height around the caldera varies with different initial conditions, primarily the relationship between the explosion energy, E, and the initial maximum water elevation, η_i (Table 3). An explosive crater with an initially strong peak that has a maximum height of η_i at a watery rim rapidly collapses. Then, the water rushes inward under the influence of gravity, and a positive leading

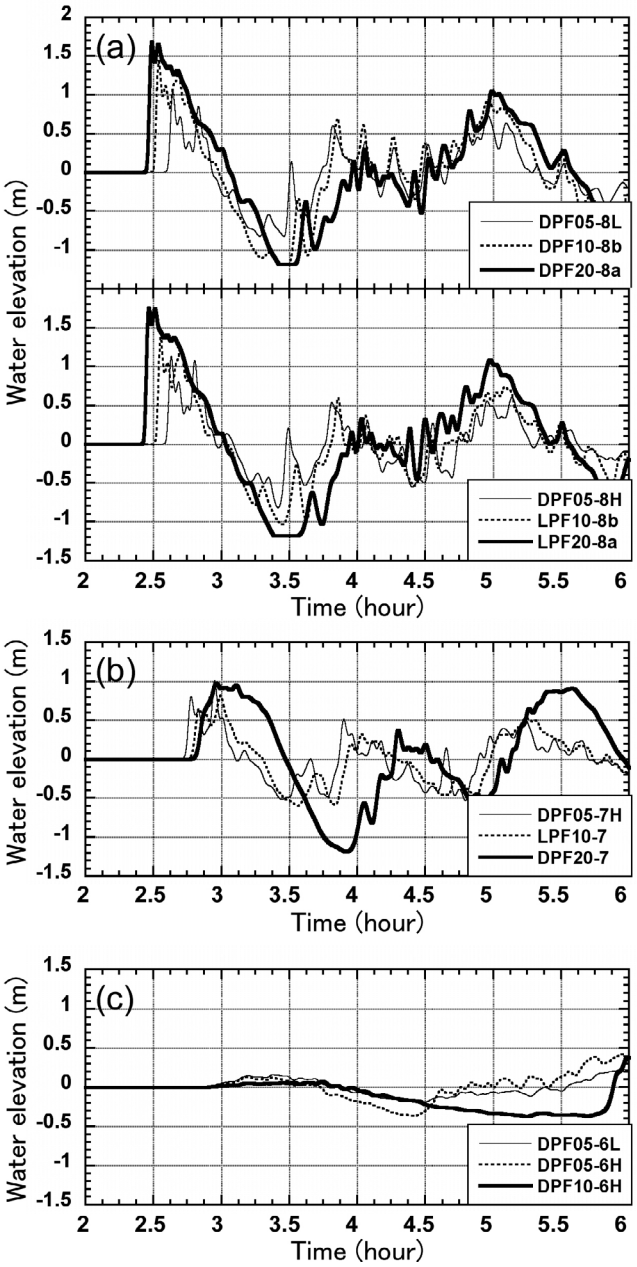

Figure 10. Computed waveforms of tsunamis at Batavia, using pyroclastic flow models with different initial condition. (a–c) Results using an average flux of 10^8 m^3/s, 10^7 m^3/s, and 10^6 m^3/s. See Table 1 for model details. The time is from the pyroclastic flow generation at the source.

wave is created toward the outside of the crater (Figure 13). The local reduction in sea level following the first wave crest caused by the inrush of water is transmitted outwards as a long shallow wave trough. As a result, a tsunami is generated with a first positive peak and negative leading peaks; however, the first peak cannot keep its original height as it is rapidly attenuated by seawater rushing into the crater. When the water edge of the inward motion reaches the center, a very high peak of water is thrown up (6 s in Figure 13). Subsequently, the water crater recovers and rises, due to wave collisions and an increase in the total wave height as observed in the caldera collapse models. Even if the initial water elevation (η_0) is over 200 m, it still rapidly decreases.

[41] Results using model PME4 with an explosion energy of 10^{17} J are shown as an example (Figures 8e and 8f), where the first positive peak reached PRI in 25 min, ANJ in 33 min and KAL in 38 min. A typical waveform shows a positive peak followed by a negative one, which has the same sense as the results from a model of a pyroclastic flow entering the sea. Although computed tsunamis show differences in maximum wave heights and arrival times with different explosion energy, there are no significant differences in the shapes of the waveforms (Figure 14).

6. Discussion

6.1. Comparison of Numerical Data With a Tidal Gauge Record at Batavia

[42] Computed wave characteristics were compared with records from coastal locations where wave data were measured and estimated immediately after the eruption [*Verbeek*, 1885; *Symons*, 1888]. The most important location is Batavia on the north coast of Java, where a tidal gauge recorded the largest and subsequent tsunamis with decreasing amplitude. The first positive peak arrived at 12:30 on 27 August (Krakatau local time, equivalent to 12:36 at Batavia) following a gradual increase of sea level (Figure 15a). A rise in sea level at 12:15 arrived as almost a wall of water, as the first wave inundated the shore [*Symons*, 1888]. This wave attained a height of more than 1.6 m above sea level at 12:36. It then rapidly fell to less than 0.23 m below the sea level. These water elevation changes were measured by Verbeek, who stated that the gauge would not register the full range of the wave. The diagram shows only +1.60 m and −0.23 m, and the minimum value appears doubtful as no explanation of how the observations for the minimum were taken was provided beyond the statement that they were made relative to fixed points in the port [*Symons*, 1888].

[43] The travel time of the tsunami was about 2 h 30 min from the most intense eruption at 10:02. A maximum wave height at Batavia was at least 1.8 m and the wave period was about 2 h [*Symons*, 1888; *Simkin and Fiske*, 1983]. Computed tsunami waveforms from representative initial conditions for the three hypotheses presented (models DPF10–8, CC30, and PME4) are shown in Figures 15b–15d. The selected simulations are those whose results are closer to the observation. Comparing these results with recorded data at Batavia, tsunamis generated by a pyroclastic flow entering the sea match the tidal gauge record well, in terms of its waveform. Only model DPF10–08 is shown in Figure 15, but this feature of waveform is common for other initial conditions—particularly for models with an average volume flux of 10^7 to 10^8 m^3/s (Figure 10). A wave period of about 2 h can also be reproduced by stand-alone pyroclastic flow models (Figures 10 and 15).

[44] Numerical results using caldera collapse models showed negative peak arrivals first (Figures 12 and 15c), which is consistent with the results of *Nomanbhoy and Satake* [1995]. This wave characteristic has a completely opposite sense to the case of a model of a pyroclastic flow entering the sea.

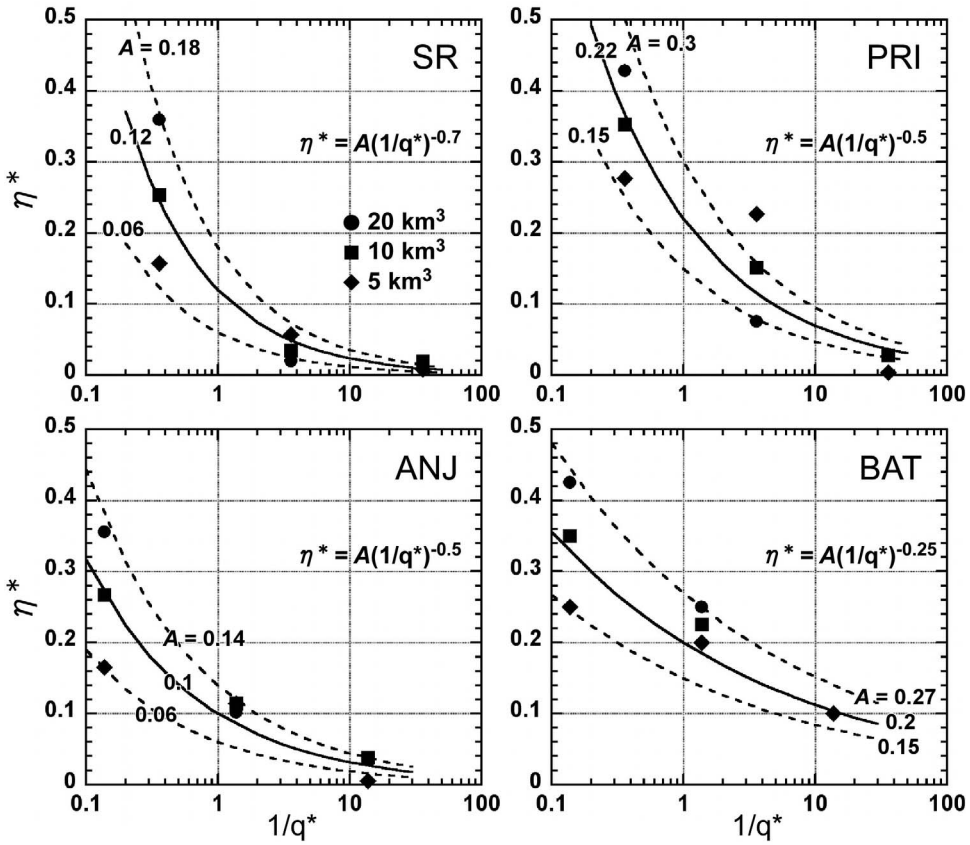

Figure 11. Relationship between the reciprocal of the non-dimensional average volume flux of pyroclastic flow ($1/q^* = \sqrt{gh_p}/Q'_{ave}$) and the non-dimensional wave amplitude of the tsunami ($\eta^* = \eta/h_d$) for four representative locations: SR (near-field), and 2 to 3 km offshore from PRI, ANJ, and BAT (far-field). Q'_{ave} is an average volume flux per unit width at the source, h_p is water depth near the end of proximal submarine flow motion, h_d is the distal water depth at the location where the wave amplitude is collected.

The results from the caldera collapse model cannot explain the wave data at Batavia, where the positive wave arrived first.

[45] For the phreatomagmatic explosion model, a positive first peak and negative leading peaks agree with field observations. This pattern also occurs for pyroclastic flows entering the sea, but short period components are more dominant than long period ones, and the maximum wave height is much lower than for field observation (Figures 14 and 15d). Numerical simulations suggest that even if the initial elevation of a watery crater rim reached 200 to 300 m by a potential huge submarine explosion (with an energy of 10^{16} to 10^{17} J), the wave height would decrease rapidly and large tsunamis would be unlikely to be generated. *Nomanbhoy and Satake* [1995] used a simple water displacement model to simulate an initial water dome. Although their computed waveforms may explain some of the observations made at Batavia, this approximation was not based on the physical considerations of underwater explosions and the computed arrival times of tsunamis are slightly later than for the actual observations. Some of wave heights at other coastal locations along the Sunda Strait cannot also explain the data obtained by *Symons* [1888] as discussed in the next section. These discrepancies are assumed to have been derived from unrealistic initial conditions.

[46] The tidal gauge record shows that a first positive peak arrived at 12:36 at Batavia. If we assume that the voluminous pyroclastic flow coincidently occurred with the explosion at 10:02, the traveling time of tsunami should be 2.5 h. In fact, we cannot determine an accurate time for the pyroclastic flow generation and the traveling time of tsunami. If the pyroclastic flow was produced by an event that followed the intense explosion, like column collapse, it would have caused a time gap between the 10:02 explosion and the pyroclastic flow. Moreover, in our simulation, the peak flux of the pyroclastic flow comes at a half of duration ($T/2$), because we used a sine source function (Figure 4). This effect of the source function on the timing of the peak discharge rate may have caused some inconsistencies between observations and numerical results. In Figure 10, computed waveforms calculated using three different average fluxes of pyroclastic flow, 10^8, 10^7 and 10^6 m^3/s are shown. Taking the difficulty of determining the accurate traveling time of a tsunami into account, we propose that pyroclastic flows with an average flux of 10^7 to 10^8 m^3/s are more appropriate to account for the tsunami recorded at Batavia, in terms of arrival times

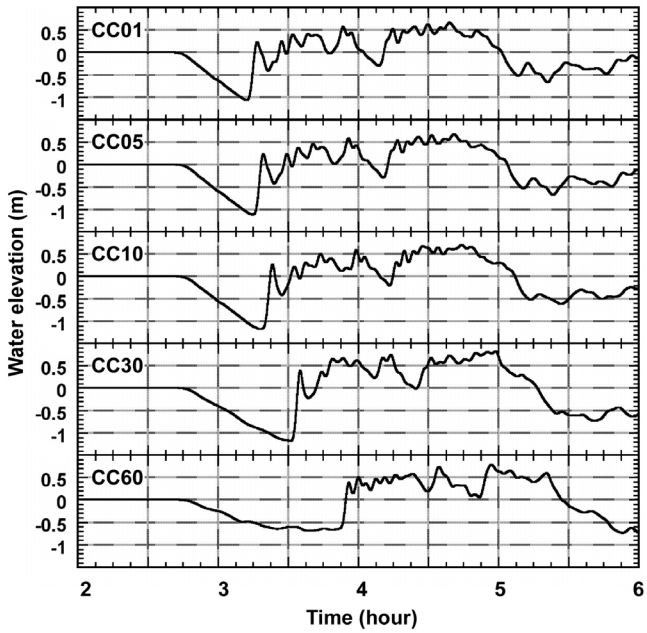

Figure 12. Computed waveforms at Batavia for caldera collapse models with different initial condition. See Table 2 for model details. The time is from the beginning of collapse.

and waveforms (Figures 10a and 10b). For a pyroclastic flow with an average flux of 10^6 m^3/s, the waveforms with a first positive peak and following perturbations have the same sense; however, the arrival time may be too late and the amplitude of the first wave is too small. The model does not match the recorded wave characteristics (Figure 10c).

[47] Although one of the causes for the occurrence of successive peaks with a long wave period of about 2 h [*Symons*, 1888] has been attributed to a sequence of events, our numerical results also explain that such a long wave period could be caused by rebounds of the first (and highest) wave generated by a single pyroclastic flow event, based on tracing the paths of wave peaks of the tsunami in Sunda Strait.

[48] The mass discharge rate of a pyroclastic flow is thought to be crucial to the determination of resultant wave characteristics for tsunamis, as shown in Figures 9 and 10. However, other physical parameters may also affect tsunami behavior. Therefore, we also compared various tsunami waveforms at Batavia, which are calculated from different flow densities and drag coefficients (Figure 16). Under conditions with the same flux and a volume of 5 km^3, the resultant waveforms are almost the same over a range of densities from 1100 to 1500 kg/m^3 (Figures 16a and 16b). In cases with a volume of 10 km^3, a density difference may slightly affect the resultant waveforms (Figure 16c; models LPF10–7 and DPF10–7H). The effects of differences of friction coefficients, n_a (0.01 or 0.06 for subaerial flows), n_m (0.06 or 0.08 for submarine flows), and f (0.06 to 0.20), were also examined. However, they do not produce significant differences among the results (Figures 16c and 16d). The effects of flux, volume, and density are more significant on tsunami wave characteristics beyond the range of drag coefficients.

6.2. Comparison of Numerical Data With Coastal Records

[49] Computed wave heights at coastal locations around Sunda Strait (Figure 1) can be compared with data obtained by *Symons* [1888]. Actual runup heights were measured immediately after the eruption by *Verbeek* [1885], then wave heights were estimated by *Symons* [1888] using these data. Here we compare only wave height data with our numerical results, because of the difficulties of numerically constraining the runup heights of tsunamis. Uncertainty of the precise locations where the tsunami runup actually occurred and the relatively coarse grid near the coasts in our simulation make it difficult to accurately calculate runup heights. Moreover, we use only results from pyroclastic flow models because in our simulation caldera collapse (CC) and phreatomagmatic explosion (PME) models cannot explain the Batavia data at all.

[50] Computed wave heights of tsunamis are shown for 12 locations with different initial conditions (Figure 17).

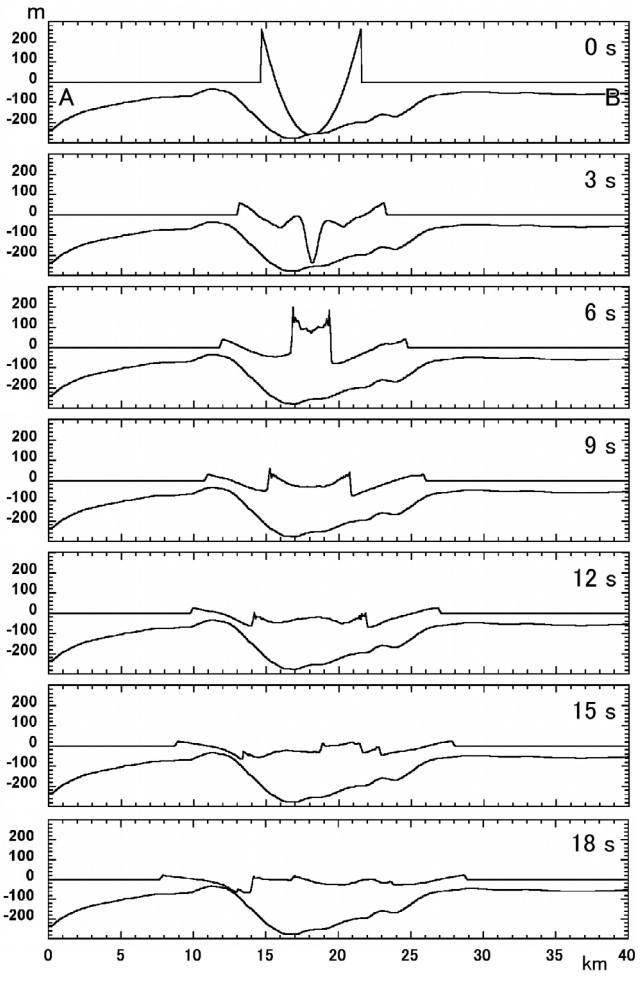

Figure 13. Wave height profiles of a tsunami generated by a phreatomagmatic explosion where the PME4 model (with explosion energy of 10^{17} J and a 7 km diameter crater) was used. The profiles correspond to line A-B in Figure 5.

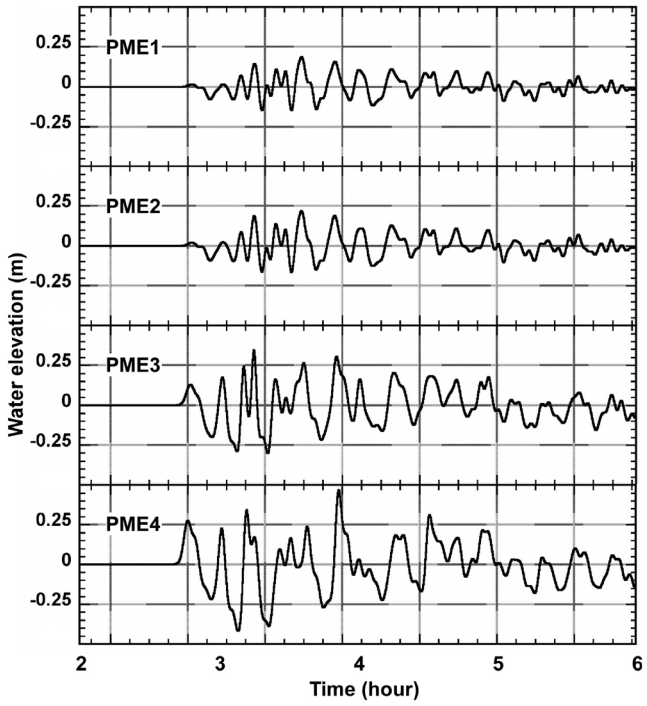

Figure 14. Computed waveforms at Batavia for phreatomagmatic explosion models with different initial condition. See Table 3 for model details.

Symons [1888] estimated wave heights to be about 15 m for many near-source locations and a few meters for the northern coast of Java. The numerical results of *Nomanbhoy and Satake* [1995] are also shown. They concluded that their phreatomagmatic explosion model can explain Symons' data better than other models, and therefore suggest that this is the most plausible mechanism. Nevertheless, there are discrepancies at some locations, such as MER, KAL, BEL, BAN, KRA and THO (Figure 17). Our numerical results using pyroclastic flow models are compared with the data from *Symons* [1888] and the results of *Nomanbhoy and Satake* [1995], although indeed the adoption of the 15 m value for all the near-field measurements appears to be questionable. When DPF05–7 or 05–8 models are used (Figures 17a and 17b), our results are much closer to the Symons' data, although they are slightly higher at PRI and lower at KRA and THO. When a flow volume of 10 km^3 was used (Figures 17c and 17d), model DPF10–7H, with the highest flow density among the same flux models, produced results closest to the Symons' data. An average flux of 10^8 m^3/s resulted in tsunami heights that were too high, and those from an average flux of 10^6 m^3/s were too low. When a flow volume of 20 km^3 was modeled, the results were inconsistent with Symons' data (Figures 17e and 17f). Further examination of different conditions between the two cases may obtain other matching results, where the average volume flux is on the order of 10^7 m^3/s.

[51] Although our numerical results using pyroclastic flow models are the most consistent with recorded data, the results do not completely match. This may, in part, be due to uncertainties in Verbeek and Symons' data. *Symons* [1888] showed tsunami wave heights based on Verbeek's data, but

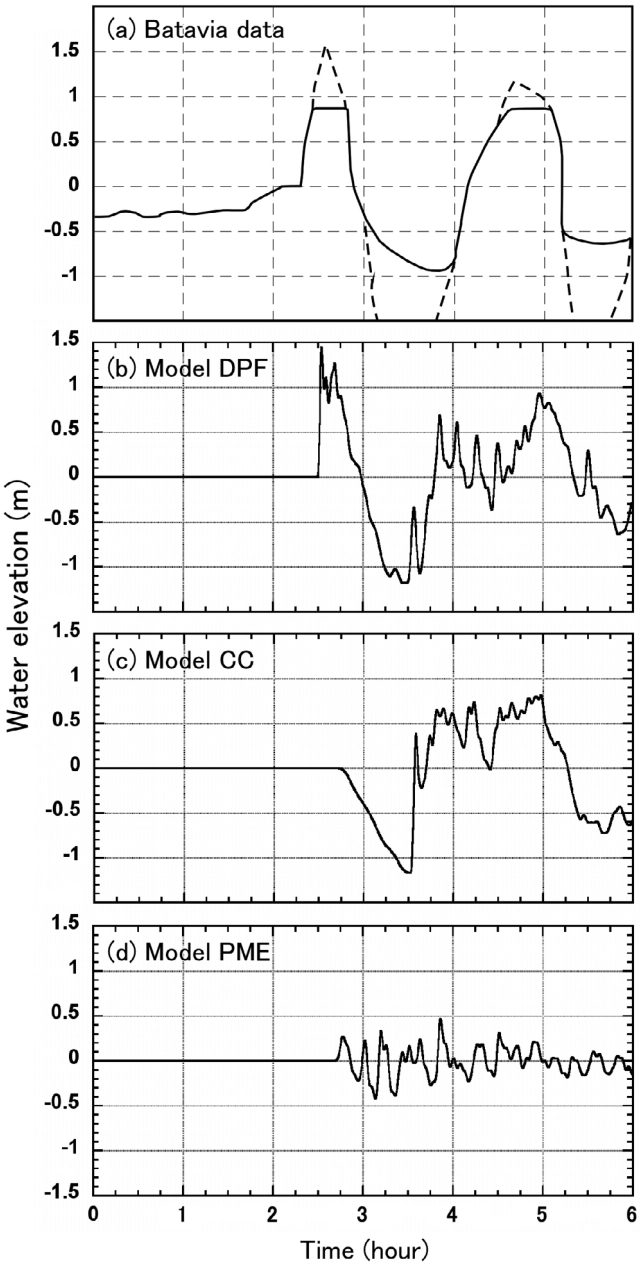

Figure 15. (a) Observed tsunami waveform at the Batavia tide gauge station and representative computed tsunami waveforms from three different models: (b) pyroclastic flow model (DPF10–08b), (c) caldera collapse model (CC30), (d) phreatomagmatic explosion model (PME4). The observed tsunami is characterized by an initial positive peak and successive peaks of decreasing amplitude. The first positive peak arrived in 2.5 h after the 10:02 explosion, with a wave height of at least 1.8 m (minimum estimation) and a wave period of about 2 h. The dashed line indicates the water elevation changes measured by *Verbeek* [1885] (see text for the detail). The computed waveform from a pyroclastic flow model has similar characteristics to the observed waveform.

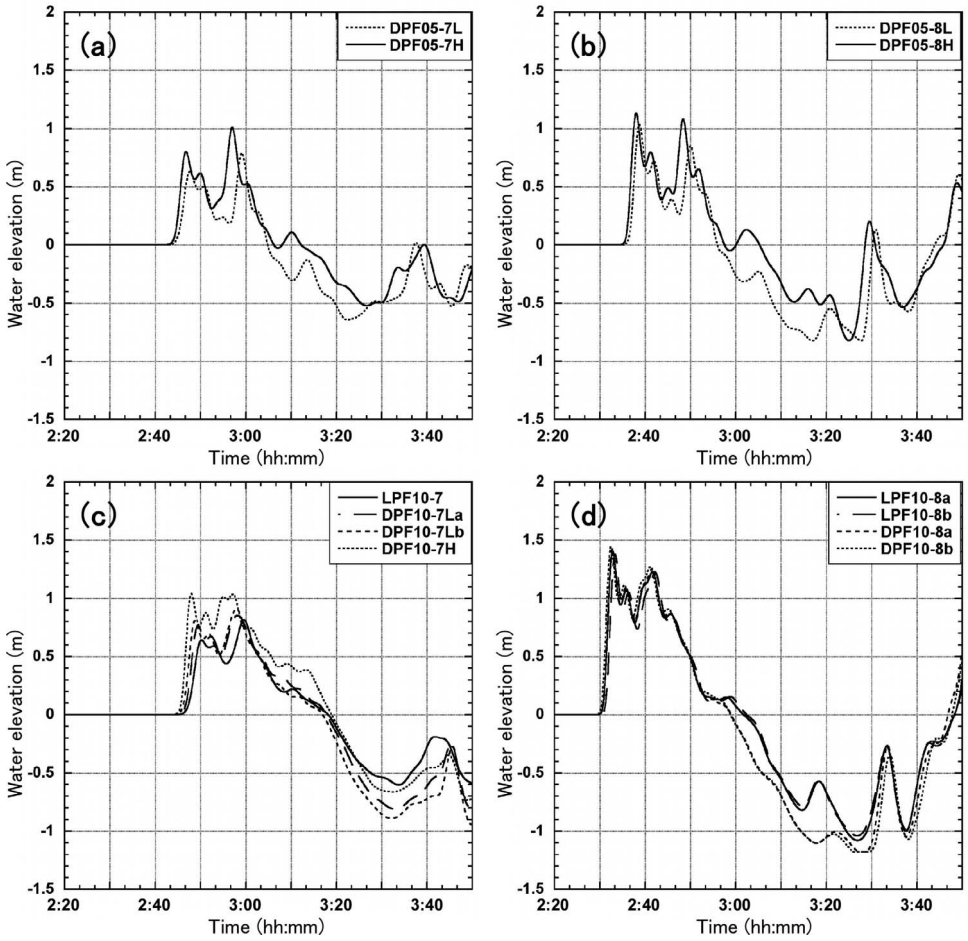

Figure 16. Comparison of tsunami waveforms at Batavia using different initial conditions with average fluxes of (a) 10^7 m^3/s and (b) 10^8 m^3/s, and with flow densities of 1100 kg/m^3 (L) and 1500 kg/m^3 (D). The volume is constant (5 km^3). Comparison of tsunami waveforms at Batavia using different initial conditions with different flow densities (900 to 1500 kg/m^3) and drag coefficients (see Table 1) using models with an average flux of (c) 10^7 m^3/s and a volume of 10 km^3 and (d) 10^8 m^3/s and a volume of 10 km^3.

for all coastal locations near the source these were estimated to be 15 m—and the accuracy of this estimate is unclear. Some reasonable errors should be taken into account here. Another possible reason for the discrepancies is the grid size in our numerical simulation. Some complex coastal lines may be beyond the resolution of our simulation. For example, according to *Symons* [1888], the tsunami wave height reached 15 m in the south of Sumatra. However, none of our results for any of the three source hypotheses can explain this height; *Nomanbhoy and Satake* [1995] were unable to explain this height either.

6.3. Comparison of Numerical Data With Submarine Pyroclastic Flow Deposits

[52] Submarine pyroclastic flow deposits around the Krakatau Islands are another important clue to evaluate the source condition of pyroclastic flows and tsunamis. Our numerical simulation does not consider particle sedimentation within the pyroclastic flow, but the spreading behavior of such a flow is comparable with the observed distribution of a submarine ignimbrite (Figure 2d). Representative examples of the resultant distributions of dense and light pyroclastic flows were shown in Figure 6.

[53] The flow was mainly distributed in the north, west and southwest. To the west of Rakata Island, the deposit became the thickest, and in the southeast is the thinnest (Figure 6). This general trend, which appears in all parameter studies, is consistent with a major distribution of submarine ignimbrite, although it cannot explain some flow deposits that are identified on the southwest of Rakata Island with a thickness of more than 50 m [*Sigurdsson et al.*, 1991; *Mandeville et al.*, 1994, 1996]. The reason for less deposition in the southeastern area is due to a topographic effect of the old Rakata Island on pyroclastic flow spreading. The island had a high peak in the south that would have acted as a significant obstacle to mass transport.

[54] One important observation is that pyroclastic flows bypassed an annular moat of surrounding basins, especially prominent on the northern side between Steers or Calmeyer and Krakatau (Figures 2b and 2d) [*Simkin and Fiske*, 1983; *Sigurdsson et al.*, 1991]. *Legros and Druitt* [2000] suggested that pyroclastic flows of 10 km^3 or more are capable

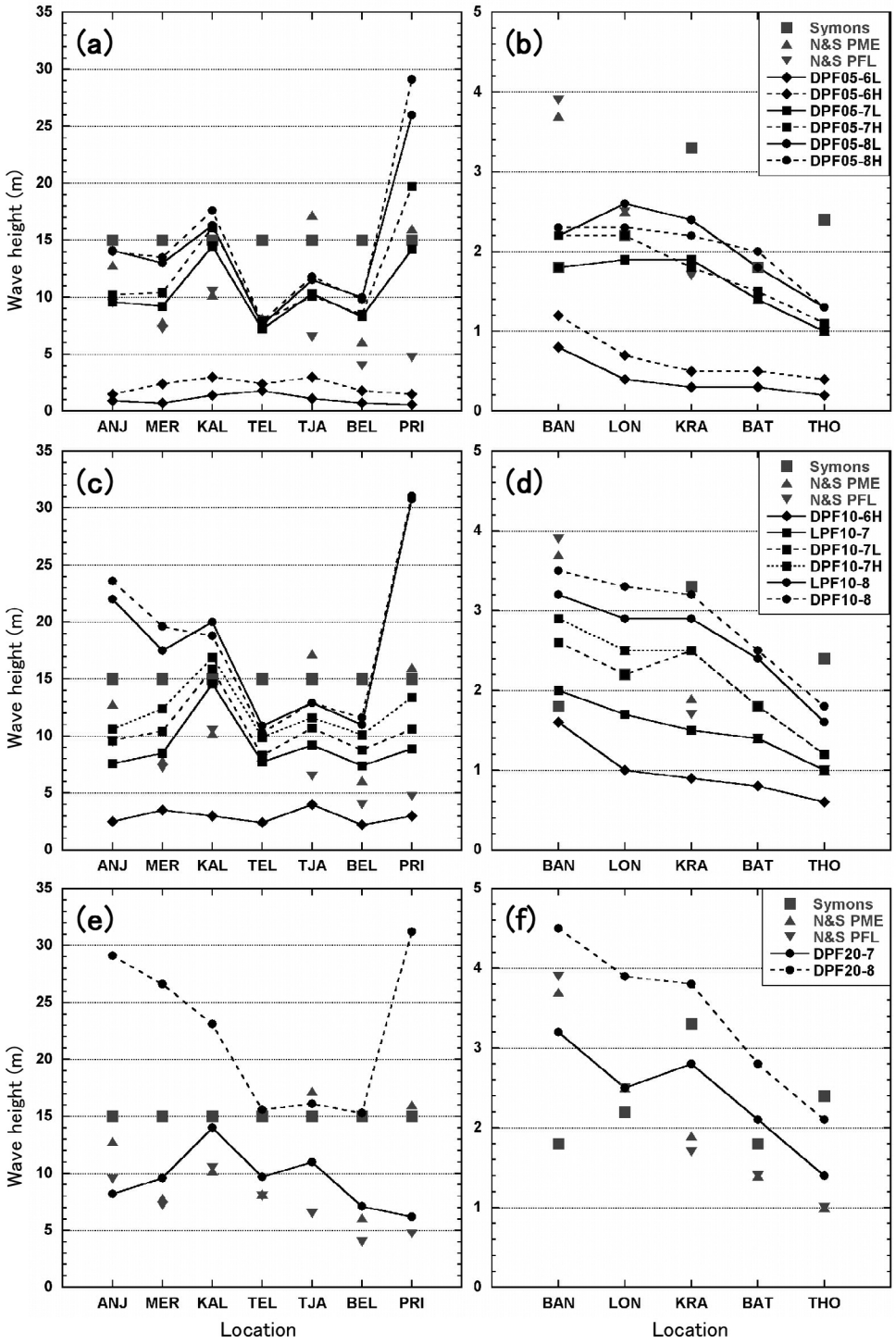

Figure 17. Comparison of tsunami wave heights calculated in this study (black symbols) with estimates of *Symons* [1888] (gray squares) and results of *Nomanbhoy and Satake* [1995] (N&S, gray triangles; PME, phreatomagmatic explosion model; PFL, pyroclastic flow model). Left and right figures show wave heights for proximal and distal locations, respectively. (a and b) Results from models with a volume of 5 km^3. (c and d) Results from models with a volume of 10 km^3. (e and f) Results from models with a volume of 20 km^3.

of pushing back the sea at least a couple of kilometers in areas of extensive shallow water, and that the mass flux necessary to temporally sweep the sea off the shelf as much as 10 km from Krakatau, as historically recorded, is greater than 10^{10} kg/s for a circular source. Our numerical results using a lighter-type model (Figures 6d and 6f) showed that pyroclastic flows could sweep the sea off the shallow platform at the north and west of the source (Figures 7b and 7d).

Although the density evolution of pyroclastic flows cannot be precisely determined, the results support this idea of sweeping the sea off, and also simultaneously explain observed tsunami data at coastal locations, including Batavia (Figure 10). Taking the distribution of computed flows (Figure 6) into account, a volume of 5 km^3 may be too little to reproduce the observed deposits in the north of Krakatau.

[55] The most plausible condition is that a pyroclastic flow with a volume of >5 km^3 and an average flux of the order of 10^7 m^3/s rapidly entered the sea. The mass flux at the source depends on the initial flow density. Assuming flow density of about 1000 kg/m^3 or less, the required mass flux could be the order of 10^9 to 10^{10} kg/s. The range of the initial flux is consistent with those estimated for relatively large-scale caldera-forming eruptions, but maybe a little larger than those for smaller caldera-forming eruptions. For example, mass discharge rates for VEI 7 class large eruptions are estimated to be on the order of 10^{10} kg/s [e.g., *Bursik and Woods*, 1996]; 2 to 8×10^{10} kg/s for the Taupo eruption [*Wilson and Walker*, 1985; *Dade and Huppert*, 1996], 1.2 to 4.8×10^{10} kg/s for the Campi Flegrei eruption [*Rosi et al.*, 1996], and 0.5 to 2×10^{10} kg/s for the Bishop Tuff eruption [*Wilson and Hildreth*, 2003]. The 1815 Tambora and the Minoan (Santorini) eruptions are also VEI 7, but they are estimated to be about 1.4×10^9 kg/s [*Self et al.*, 1984] and 1.2×10^9 kg/s [*Wilson*, 1980], respectively. The peak mass flux during the 1991 Mount Pinatubo eruption was estimated to be 1 to 2×10^9 kg/s [*Scott et al.*, 1996]. In addition, our model assumes that the flows spread radially over 360° from an ideal circular source, but in fact they could be focused at the northern part of the caldera between two islands (Sertung and Panjang) and at the western part (Figure 2). If the flow was directional and concentrated over these parts, the required flux may fall by as much as half or one order, as discussed by *Legros and Druitt* [2000]. Even if the flux decreased, it is likely that ignimbrite was emplaced in a short period during high-intensity explosions.

[56] The rapid discharge of a pyroclastic flow is the most likely mechanism for the largest tsunami observed at Batavia, but actually all three processes (pyroclastic flows, phreatomagmatic explosion and caldera collapse) might have occurred and their effects may have combined during the climactic phase of the eruption. Some historical and geological observations suggest that littoral explosions can occur when pyroclastic flows encounter the sea [e.g., *Cas and Wright*, 1991; *Edmonds and Herd*, 2005]. In our model of pyroclastic flows, kinetic interactions between the flow and the water were assumed to be a major process, but thermal interactions, in which mass and heat transfers are coupled, were not considered. This may also contribute to an increase in the tsunami wave height [*Watts and Waythomas*, 2003; *Dufek et al.*, 2007] and may even explain discrepancies between observations and numerical results.

7. Conclusions

[57] The 1883 Krakatau eruption provides the best opportunity for understanding the generation and propagation processes of devastating volcanogenic tsunamis and their source conditions. Three major hypotheses for the tsunami generation mechanism of this eruption, pyroclastic flow entering sea, caldera collapse and submarine phreatomagmatic explosion, were examined by numerical simulation. For the pyroclastic flow hypotheses, two types of two-layer shallow water models (a dense-type model and a light-type model) were used under different initial conditions, in which a volume of 5 to 20 km^3 of pyroclastic flow with densities of 900 to 1500 kg/m^3 and average discharge rates of 10^6 to 10^8 m^3/s were examined. Pyroclastic flows were erupted from a circular source at the north of old Rakata Island, with a sine-function source that assumes waning and waxing phases. The caldera collapse hypothesis used a simple piston-like plunger model, in which collapse duration was assumed to be 1 min to 1 h. The phreatomagmatic explosion hypothesis used simple empirical models for underwater explosions in shallow water, with initial condition including an explosion crater radius of 2 to 3.5 km and explosion energy of 10^{16} and 10^{17} J.

[58] Tsunami wave heights computed at coastal locations along Sunda Strait, using the first hypothesis of pyroclastic flow entering sea, matched well with the data estimated from historical records. In fact, the results matched better than previously published work based on a different tsunami-generation process. At Batavia, on the northern coast of Java, the first positive peak reached within 2.5 h with a long wave period (about 2 h). These wave characteristics are consistent with records from a tide-gauge station there. In comparison, caldera collapse and phreatomagmatic explosion models cannot explain observed data, either in terms of the tide-gauge records at Batavia or wave heights in coastal areas. Our results suggest that the pyroclastic flow entering sea, with a volume of more than 5 km^3 and an average discharge rate of the order of 10^7 m^3/s, would be the most plausible mechanism of the large tsunami during the 1883 Krakatau eruption.

[59] **Acknowledgments.** The authors thank A. Armigliato and an Associate Editor for constructive reviews, and R.S.J. Sparks for helpful comments. F.M. was supported by a grant-in-aid for young scientists (B) (19710150) from the Ministry of Education, Culture, Sports Science and Technology (MEXT), Japan.

References

Allen, S. R., and R. A. F. Cas (2001), Transport of pyroclastic flows across the sea during the explosive, rhyolitic eruption of the Kos Plateou Tuff, Greece, *Bull. Volcanol.*, *62*, 441–456, doi:10.1007/s004450000107.

Amante, C., and B. W. Eakins (2009), ETOPO1 1 Arc-Minute Global Relief Model: Procedures, data sources and analysis, *NOAA Tech. Memo. NESDIS NGDC*, *24*, 19 pp.

Beget, J. E. (2000), Volcanic tsunami, in *Encyclopedia of Volcanoes*, edited by H. Sigurdsson, pp. 1005–1013, Elsevier, New York.

Bursik, M. I., and A. W. Woods (1996), The dynamics and thermodynamics of large ash flows, *Bull. Volcanol.*, *58*, 175–193, doi:10.1007/s004450050134.

Camus, G., and P. M. Vincent (1983), Discussion of a new hypothesis for the Krakatau volcanic eruption in 1883, *J. Volcanol. Geotherm. Res.*, *19*, 167–173, doi:10.1016/0377-0273(83)90130-0.

Carey, S., H. Sigurdsson, C. Mandeville, and S. Bronto (1996), Pyroclastic flows and surges over water: An example from the 1883 Krakatau eruption, *Bull. Volcanol.*, *57*, 493–511, doi:10.1007/BF00304435.

Carey, S., H. Sigurdsson, C. Mandeville, and S. Bronto (2000), Volcanic hazards from pyroclastic flow discharge into the sea: Examples from 1883 eruption of Krakatau, Indonesia, in *Volcanic Hazards and Disasters in Human Antiquity*, edited by F. W. McCoy and G. Heiken, pp. 1–14, Geol. Soc. of Am., Boulder, Colo., doi:10.1130/0-8137-2345-0.1.

Carey, S., D. Morelli, H. Sigurdsson, and S. Bronto (2001), Tsunami deposits from major explosive eruptions: An example from the 1883 eruption of Krakatau, *Geology*, *29*, 347–350, doi:10.1130/0091-7613(2001)029<0347:TDFMEE>2.0.CO;2.

Cas, R. A. F., and J. V. Wright (1991), Subaqueous pyroclastic flows and ignimbrites: An assessment, *Bull. Volcanol.*, *53*, 357–380, doi:10.1007/BF00280227.

Choi, B. H., E. Pelinovsky, K. O. Kim, and J. S. Lee (2003), Simulation of the trans-oceanic tsunami propagation due to the 1883 Krakatau volcanic eruption, *Nat. Hazards Earth Syst. Sci.*, *3*, 321–332, doi:10.5194/nhess-3-321-2003.

Dade, W. B., and H. E. Huppert (1996), Emplacement of the Taupo ignimbrite by a dilute turbulent flow, *Nature*, *381*, 509–512, doi:10.1038/381509a0.

De Lange, W. P., G. S. Prasetya, and T. R. Healy (2001), Modeling of tsunamis generated by pyroclastic flows (Ignimbrites), *Nat. Hazards*, *24*, 251–266, doi:10.1023/A:1012056920155.

De Rooij, F., P. F. Linden, and S. B. Dalziel (1999), Saline and particle-driven interfacial intrusions, *J. Fluid Mech.*, *389*, 303–334, doi:10.1017/S0022112099005078.

Deplus, C., S. Bonvalot, D. Dahrin, M. Diament, H. Harjono, and J. Dubois (1995), Inner structure of the Krakatau volcanic complex (Indonesia) from gravity and bathymetry data, *J. Volcanol. Geotherm. Res.*, *64*, 23–52, doi:10.1016/0377-0273(94)00038-I.

Druitt, T. H. (1997), Pyroclastic density currents, in *The Physics of Explosive Volcanic Eruptions*, edited by J. S. Gilbert and R. S. J. Sparks, pp. 145–182, Geol. Soc., London.

Dufek, J., and G. W. Bergantz (2007), Dynamics and deposits generated by the Kos Plateau Tuff eruption: Controls of basal particle loss on pyroclastic flow transport, *Geochem. Geophys. Geosyst.*, *8*, Q12007, doi:10.1029/2007GC001741.

Dufek, J., M. Manga, and M. Staedter (2007), Littoral blasts: Pumice-water heat transfer and the conditions for steam explosions when pyroclastic flows enter the ocean, *J. Geophys. Res.*, *112*, B11201, doi:10.1029/2006JB004910.

Edmonds, M., and R. A. Herd (2005), Inland-directed base surge generated by the explosive interaction of pyroclastic flows and seawater at Soufriere Hills volcano, Montserrat, *Geology*, *33*(4), 245–248, doi:10.1130/G21166.1.

Ewing, M., and F. Press (1955), Tide-gauge disturbances from the great eruption of Krakatoa, *Eos Trans. AGU*, *36*, 53–60.

Fisher, R. V., G. Orsi, M. Ort, and G. Heiken (1993), Mobility of a large-volume pyroclastic flow—Emplacement of the Campanian ignimbrite, Italy, *J. Volcanol. Geotherm. Res.*, *56*, 205–220, doi:10.1016/0377-0273(93)90017-L.

Francis, P. W. (1985), The origin of the 1883 Krakatau tsunamis, *J. Volcanol. Geotherm. Res.*, *25*, 349–363, doi:10.1016/0377-0273(85)90021-6.

Freundt, A. (2003), Entrance of hot pyroclastic flows into the sea: Experimental observations, *Bull. Volcanol.*, *65*, 144–164.

Goto, C., and N. Shuto (1983), Numerical simulatiom of tsunami propagation and runup, in *Tsunami - Their Science and Engineering*, edited by K. Iida and T. Iwasaki, pp. 439–451, Terrapub, Tokyo.

Goto, C., Y. Ogawa, N. Shuto, and F. Imamura (1997), IUGG/IOC time project, Numerical method of tsunami simulation with the leap-frog scheme, *IOC Manuals and Guides*, *35*, 130 pp., U.N. Educ. Sci. Cult. Organ., Paris.

Imamura, F., and M. A. Imteaz (1995), Long waves in two-layers: Governing equations and numerical model, *Sci. Tsunami Hazards*, *13*(1), 3–24.

Kawamata, K., K. Takaoka, K. Ban, F. Imamura, S. Yamaki, and E. Kobayashi (2005), Model of tsunami generation by collapse of volcanic eruption: The 1741 Oshima-Oshima tsunami, in *Tsunamis: Case Studies and Recent Development*, edited by K. Satake, pp. 79–96, Springer, New York.

Kawamata, S., F. Imamura, and N. Shuto (1993), Numerical simulation of the 1883 Krakatau tsunami, paper presented at XXV Congress, Int. Assoc. Hydroenviron. Eng., Tokyo.

Lane, E. W., and A. A. Kalinske (1941), Engineering calculations of suspended sediment, *Eos Trans. AGU*, *22*, 603–607.

Latter, J. H. (1981), Tsunamis of volcanic origin: Summary of causes, with particular reference to Krakatoa, 1883, *Bull. Volcanol.*, *44*, 467–490, doi:10.1007/BF02600578.

Le Mehaute, B., and T. Khangaonkar (1992), Generation and propagation of explosion generated waves in shallow water, *Tech. Rep. DNA-TR-92–40*, Nucl. Def. Agency, Washington D. C.

Le Mehaute, B., and S. Wang (1996), *Water Waves Generated by Underwater Explosion*, *Adv. Ser. Ocean Eng.*, vol. 10, 367 pp., World Sci., New Jersey.

Legros, F., and T. H. Druitt (2000), On the emplacement of ignimbrite in shallow-marine environments, *J. Volcanol. Geotherm. Res.*, *95*, 9–22, doi:10.1016/S0377-0273(99)00116-X.

Maeno, F., and F. Imamura (2007), Numerical investigations of tsunamis generated by pyroclastic flows from the Kikai caldera, Japan, *Geophys. Res. Lett.*, *34*, L23303, doi:10.1029/2007GL031222.

Maeno, F., and H. Taniguchi (2007), Spatiotemporal evolution of a marine caldera-forming eruption, generating a low-aspect ratio pyroclastic flow, 7.3 ka, Kikai caldera, Japan: Implication from near-vent eruptive deposits, *J. Volcanol. Geotherm. Res.*, *167*, 212–238, doi:10.1016/j.jvolgeores.2007.05.003.

Maeno, F., F. Imamura, and H. Taniguchi (2006), Numerical simulation of tsunamis generated by caldera collapse during the 7.3 ka Kikai eruption, Kyushu, Japan, *Earth Planets Space*, *58*(8), 1013–1024.

Mandeville, C. W., S. Carey, H. Sigurdsson, and J. King (1994), Paleomagnetic evidence for high-temperature emplacement of the 1883 subaqueous pyroclastic flows from Krakatau volcano, Indonesia, *J. Geophys. Res.*, *99*(B5), 9487–9504, doi:10.1029/94JB00239.

Mandeville, C. W., S. Carey, and H. Sigurdsson (1996), Sedimentology of the Krakatau 1883 submarine pyroclastic deposits, *Bull. Volcanol.*, *57*, 512–529, doi:10.1007/BF00304436.

Matsumoto, T., K. Hashi, F. Imamura, and N. Shuto (1998), Development of tsunami generation and propagation model by debris flow (in Japanese), paper presented at 45th Coastal Engineering Conference, Japan Soc. of Civ. Eng., Tokyo.

McLeod, P., S. Carey, and R. S. J. Sparks (1999), Behaviour of particle-driven flows into the ocean: Experimental simulation and geological implications, *Sedimentology*, *46*, 523–536, doi:10.1046/j.1365-3091.1999.00229.x.

Monaghan, J. J., R. A. F. Cas, A. M. Kos, and M. Hallworth (1999), Gravity currents descending a ramp in a stratified tank, *J. Fluid Mech.*, *379*, 39–69, doi:10.1017/S0022112098003280.

Nomanbhoy, N., and K. Satake (1995), Generation mechanism of tsunamis from the 1883 Krakatau eruption, *Geophys. Res. Lett.*, *22*, 509–512, doi:10.1029/94GL03219.

Rosi, M., L. Vizzoli, P. Aleotti, and M. De Censi (1996), Interaction between caldera collapse and eruptive dynamics during the Campanian ignimbrite eruption, Phlegraean Fields, Italy, *Bull. Volcanol.*, *57*, 541–554, doi:10.1007/BF00304438.

Sato, H., and H. Taniguchi (1997), Relationship between crater size and ejecta volume of recent magmatic and phreato-mamgatic eruptions: Implications for energy partitioning, *Geophys. Res. Lett.*, *24*, 205–208, doi:10.1029/96GL04004.

Scott, W. E., R. P. Hoblitt, R. C. Torres, S. Self, M. L. Martinez, and T. J. Nillos (1996), Pyroclastic flows of the June 15, 1991, climatic eruption of Mount Pinatubo, in *Fire and Mud: Eruptions of Mount Pinatubo, Philippines*, edited by C. G. Newhall and S. Punongbayan, pp. 545–570, Philipp. Inst. Volcanol. and Seismol., Quezon City.

Self, S., and M. R. Rampino (1981), The 1883 eruption of Krakatau, *Nature*, *294*, 699–704, doi:10.1038/294699a0.

Self, S., and M. R. Rampino (1982), Comments on "A geophysical interpretation of the 1883 Krakatau eruption" by I. Yokoyama, *J. Volcanol. Geotherm. Res.*, *13*, 379–383, doi:10.1016/0377-0273(82)90058-0.

Self, S., M. R. Rampino, M. S. Newton, and J. A. Wolf (1984), Volcanological study of the great Tambora eruption of 1815, *Geology*, *12*, 659–663, doi:10.1130/0091-7613(1984)12<659:VSOTGT>2.0.CO;2.

Sigurdsson, H., S. Carey, C. Mandeville, and S. Bronto (1991), Pyroclastic flows of the 1883 Krakatau eruption, *Eos Trans. AGU*, *72*(36), 377–392, doi:10.1029/90EO00286.

Simkin, T., and R. S. Fiske (1983), *Krakatau 1883 -Eruption and Its Effects*, 464 pp., Smithson. Inst., Washington, D. C.

Symons, G. J. (1888), The eruption of Krakatau and subsequent phenomenon, Rep. of the Krakatau Comm. of the R. Soc., 494 pp., Trubner, London.

Takahashi, T., and H. Tsujimoto (2000), A mechanical model for Merapi-type pyroclastic flow, *J. Volcanol. Geotherm. Res.*, *98*, 91–115, doi:10.1016/S0377-0273(99)00193-6.

Tinti, S., G. Pagnoni, and A. Piatanesi (2003), Simulation of tsunamis induced by volcanic activity in the Gulf of Naples (Italy), *Nat. Hazards Earth Syst. Sci.*, *3*, 311–320, doi:10.5194/nhess-3-311-2003.

Torsvik, T., R. Paris, I. Didenkulova, E. Pelinovsky, A. Belousov, and M. Belousova (2010), Numerical simulation of a tsunami event during the 1996 volcanic eruption in Karymskoye lake, Kamchatka, Russia, *Nat. Hazards Earth Syst. Sci.*, *10*, 2359–2369, doi:10.5194/nhess-10-2359-2010.

U.S. Army Map Service (1954), Indonesia, *Series T503*, 1:250,000, Washington D. C.

van den Bergh, G. D., W. Boer, H. de Haas, T. C. E. van Weering, and R. van Wijhe (2003), Shallow marine tsunami deposits in Teluk Banten (NW Java, Indonesia), generated by the 1883 Krakatau eruption, *Mar. Geol.*, *197*, 13–34, doi:10.1016/S0025-3227(03)00088-4.

Verbeek, R. D. M. (1885), *Krakatau*, 495 pp., Gov. Press, Batavia, Indonesia.

Walder, J. S., P. Watts, O. E. Sorensen, and K. Janssen (2003), Tsunamis generated by subaerial mass flows, *J. Geophys. Res.*, *108*(B5), 2236, doi:10.1029/2001JB000707.

Watts, P., and C. F. Waythomas (2003), Theoretical analysis of tsunami generation by pryoclastic flows, *J. Geophys. Res.*, *108*(B12), 2563, doi:10.1029/2002JB002265.

Waythomas, C. F., and C. A. Neal (1998), Tsunami generation by pyroclastic flow during the 3500-year B.P. caldera-forming eruption of Aniakchak Volcano, Alaska, *Bull. Volcanol.*, *60*, 110–124, doi:10.1007/s004450050220.

Waythomas, C. F., and P. Watts (2003), Numerical simulation of tsunami generation by pyroclastic flow at Aniakchak volcano, Alaska, *Geophys. Res. Lett.*, *30*(14), 1751, doi:10.1029/2003GL017220.

Wilson, C. J. N., and W. Hildreth (1997), The Bishop tuff: New insights from eruptive stratigraphy, *J. Geol.*, *105*, 407–440, doi:10.1086/515937.

Wilson, C. J. N., and W. Hildreth (2003), Assembling an ignimbrite: Mechanical and thermal building blocks in the Bishop Tuff, California, *J. Geol.*, *111*, 653–670, doi:10.1086/378335.

Wilson, C. J. N., and G. P. L. Walker (1985), The Taupo eruption, New Zealand: I. General aspects, *Philos. Trans. R. Soc. A*, *314*, 199–228, doi:10.1098/rsta.1985.0019.

Wilson, L. (1980), Energetics of the Minoan eruption: Some revisions, in *Thera and the Aegean World II*, edited by C. Doumas, pp. 31–35, Thera Found, London.

Wilson, L., R. S. J. Sparks, and G. P. L. Walker (1980), Explosive volcanic eruptions IV. The control of magma properties and conduit geometry on eruption column behavior, *Geophys. J. R. Astron. Soc.*, *63*, 117–148.

Wolfe, E. W., and R. P. Hoblitt (1996), Overview of the eruptions, in *Fire and Mud: Eruptions and Lahars of Mount Pinatubo, Philipines*, edited by C. G. Newhall and R. S. Punongbayan, pp. 3–20, Univ. of Wash. Press, Seattle.

Yokoyama, I. (1981), A geophysical interpretation of the 1883 Krakatau eruption, *J. Volcanol. Geotherm. Res.*, *9*, 359–378, doi:10.1016/0377-0273(81)90044-5.

Yokoyama, I. (1987), A scenario of the 1883 Krakatau tsunami, *J. Volcanol. Geotherm. Res.*, *34*, 123–132, doi:10.1016/0377-0273(87)90097-7.

F. Imamura, Disaster Control Research Center, Graduate School of Engineering, Tohoku University, Sendai 980-8579, Japan.

F. Maeno, Department of Earth Sciences, University of Bristol, Bristol BS8 1RJ, UK. (Fukashi.Maeno@bristol.ac.uk)